Diagnosing Tropical Cyclone Intensity Variations from the Surface Wind Field Evolution

LÉO VINOUR,[a] SWEN JULLIEN,[a] AND ALEXIS MOUCHE[a]

[a] *Ifremer, Univ. Brest, CNRS, IRD, Laboratoire d'Océanographie Physique et Spatiale, IUEM, Plouzané, France*

ABSTRACT: Tropical cyclone (TC) intensity fluctuations remain a challenge for TC forecasters. Occurring through a wide range of processes, such as vortex contraction, eyewall replacements, or emission of vortex Rossby waves, they are inherently multiscale, transient, and asymmetric. In a recent study, estimates of surface wind field inner-core properties from high-resolution satellite observations were spotted as valuable for the improvement of intensity variations statistical predictability. The present study evaluates how the temporal evolution of the vortex structure, at scales ranging from $O(1)$ km to vortexwide, further provides insights on the modulation of intensity. The study is based on a set of seven realistic TC simulations with 1-km grid spacing. The surface wind field structure is studied through an original set of descriptors that characterize the radial profile, the azimuthal asymmetries, and their spectral distribution. While radial gradients evolve concurrently with intensity, the azimuthal variability of the inner core shows a stronger connection with shorter-scale intensity modulation. The increase of high-wavenumber asymmetries distributed around the ring of maximum winds is shown to precede phases of rapid (re)intensification by 5–6 h, while the concentration of asymmetry in wavenumbers 1 and 2 leads to intensity weakening. A machine learning classification finally highlights that the classification of intensification phases (i.e., intensification or weakening) can be improved by at least 11% (thus reaching ~75%) when accounting for the evolution of the radial wind gradient and the variance distribution among scales in the ring of maximum wind, relative to the sole use of vortex-averaged parameters.

SIGNIFICANCE STATEMENT: The purpose of this study is to relate changes in the surface wind field structure of tropical cyclones to their intensity variations. We design an original set of parameters to characterize the inner- and near-core contraction and asymmetry, and evaluate their connection with TC intensity modulations in a set of realistic high-resolution numerical simulations. The main outcome of our study is that opposite trends in high- and low-wavenumber variance tend to occur prior to intensity changes on short time scales, with more widespread and local-scale asymmetry corresponding to intensification, and vortex-scale polarized asymmetry corresponding to weakening. These diagnoses are shown to improve the classification of intensification and weakening phases. These results advocate for enhancing real-time high-resolution observations of surface wind fields under TCs, and using asymmetry distribution as predictors in statistical forecast models.

1. Introduction

Forecasting and understanding the life cycle of tropical cyclones (TCs) are primary concerns for meteorological science, these systems causing substantial casualties every year. While TC tracks are relatively well forecasted, maximum intensity and its variations are more difficult to predict (Elsberry et al. 2007; DeMaria et al. 2014; Emanuel and Zhang 2016). TC intensity changes can be caused by interactions of the vortex with the surrounding environment through vertical wind shear (Smith et al. 2000; Reasor et al. 2004; Corbosiero and Molinari 2002), oceanic forcing (Elsberry et al. 1976; Price 1981; Ginis 2002), and integrated atmospheric moisture (Emanuel et al. 2004; Kimball 2006; Wu et al. 2015). However, TC intensification is ultimately connected to internal dynamical processes (Montgomery and Smith 2017). The internal structure is indeed governed by complex dynamics and interacting

processes, which modulate the TC's intensity during its whole life cycle. Along with the symmetric spinup that takes place inside and above the boundary layer (BL) (Smith et al. 2009), intensification occurs notably through the merging and import of local vorticity anomalies into the parent vortex—a process termed the rotating convection paradigm—which hereby intensifies the eyewall convection (Montgomery et al. 2006). This process was observed on radar measurements by Reasor et al. (2009) as yielding to episodes of rapid intensification. Mixing of vorticity between the eye and the eyewall is a manifestation of eyewall mesovortices (Schubert et al. 1999), creating polygonal eyewalls (Lewis and Hawkins 1982; Muramatsu 1986; Menelaou et al. 2013b), and eventually leading to the generation of vortex Rossby waves (VRWs). These VRWs propagate internally to distribute perturbation energy along potential vorticity (PV) gradients, and act to restore the TC's symmetric structure and intensity (Guinn and Schubert 1993; Montgomery and Kallenbach 1997; Möller and Montgomery 1999; Wang 2002a,b; Corbosiero et al. 2006). These internal dynamics involve very localized processes, and are therefore

Corresponding author: Léo Vinour, leo.vinour@ifremer.fr

inherently asymmetric. However, they impact the radial and symmetric structure of the TC and lead to vortex-scale changes. The eye–eyewall area is thus observed as strongly varying during the TC life cycle between phases of low vorticity mixing (U-shape wind profile) favorable to rapid intensification, and phases of higher mixing (linear wind profile) with lower intensification rate (Kossin and Eastin 2001; Nguyen et al. 2011).

The response of a TC to external shear has also been related to the PV radial gradient at the critical radius (i.e., radius at which VRWs stop propagating), which is linked to the sharpness of the wind profile in the inner core (Mallen et al. 2005). The study of vortex shear resilience by Reasor et al. (2004) indeed shows how the sign of the PV gradient determines whether VRWs are damped or resonate, allowing the vortex to restore or not from a shear-caused tilt (Schecter et al. 2002; Menelaou et al. 2013a). The propagation and stagnation of VRWs is also related to the distribution and generation of rainbands. Inner rainbands are convectively coupled to propagating VRWs (Macdonald 1968; Guinn and Schubert 1993; Corbosiero et al. 2006; Li and Wang 2012), and the VRW stagnation radius coincides with the so-called rapid filamentation transition zone to outer rainbands (Rozoff et al. 2006; Wang 2008). The outer rainbands, although dynamically distinct from inner rainbands (Guinn and Schubert 1993), can in turn trigger secondary eyewall formation (Wang 2009; Guimond et al. 2020).

In addition, when the TC intensifies, radial convergence of absolute angular momentum inside the BL (due to frictional and turbulent processes) and above the BL (due to the increase of radial buoyancy gradient in conjunction with angular momentum conservation), and the diabatic heating in the eyewall lead to a contraction of the maximum wind area toward the center (Shapiro and Willoughby 1982; Stern et al. 2015) and to an expansion of the wind field at larger radii (Montgomery and Smith 2014; Kilroy et al. 2016). The outer-core expansion can also cause the formation of secondary eyewalls (Abarca and Corbosiero 2011; Abarca and Montgomery 2013), which were shown as being a restoring process for major TCs (Kuo et al. 2004, 2008; Nguyen et al. 2011). Local convective bursts generated in the eyewall are also associated to TC intensification and restoration (Steranka et al. 1986; Braun et al. 2006; Rogers 2010; Hazelton et al. 2017) as they can increase the release of latent heat in the eyewall by 25% (Kelley and Halverson 2011) and help vertically stack the vortex favoring its rapid intensification (Rogers et al. 2015). The fluctuations of intensity observed during the life cycle of a TC are thus deeply related to its internal structure, through processes that are multiscale and asymmetric in nature.

Although they are now acknowledged as essential to the understanding of TC intensity changes, internal dynamics and asymmetry diagnoses are rarely used in statistical–dynamical forecast models (Judt and Chen 2015, 2016). Low-wavenumber (WN) vortex-scale asymmetry (WN 0 and 1 of moisture, precipitation, or wind) has however been shown as important to characterize critical intensity changes and to improve predictability of TC intensity (Vukicevic et al. 2014; Bhalachandran

et al. 2019). Smaller-scale asymmetries and their impact or transfer to the vortex scale were not investigated yet, due to the limitation of observation resolution. As shown by Van Sang et al. (2008), the dynamics of mesovortices and vortical hot towers (VHTs) in the inner core, and more specifically their collective merging/segregation, are key to TC intensification. They state that VHTs and local asymmetry patterns are random in nature and introduce a high variability in the wind field evolution, hence a notable uncertainty in intensity forecasts. Diagnosing the inherent variability of inner-core asymmetric convective dynamics is thus a major challenge for forecasters, especially for statistical–dynamical modeling and rapid intensification (RI) predictions (Rozoff and Kossin 2011; Velden et al. 2010). These dynamics, being highly multiscale, transient, and quickly evolving, require both high resolution and coverage in space and time to be properly observed. Observation and modeling of the surface wind and backscatter is a consistent way to diagnose BL dynamics: the structure of mesoscale turbulent eddies (Rotunno et al. 2009) and BL rolls directly affect the surface wind field (Foster 2005; Morrison et al. 2005; Huang et al. 2018) and are central to energy exchanges between the ocean surface, the upper BL, and the vortex aloft (Guimond et al. 2018). The surface wind field is also a prominent source of information on the morphology and distortion of the eyewall, connected to eyewall axisymmetrization processes (Li et al. 2013). A recent study by Vinour et al. (2021) showed that newly available surface wind fields at 1-km resolution retrieved from synthetic aperture radars (SARs) make it possible to capture such fine-scale structures in the TC. Using a set of machine learning models to classify intensifying and decaying phases, they showed that parameters describing the sharpness of the radial wind profile and the asymmetry of the azimuthal wind distribution have the potential to improve the statistical predictability of TC intensification. The most contributing parameters to the improvement of the classification score were the asymmetry at the scale of eyewall mesovortices (wavenumbers 4 and 5) and eye–eyewall mixing. The study was however limited by the sparsity of acquisitions, which prevented the authors from diagnosing the temporal changes in the internal structure.

The present work follows on their study, using a dynamical model to simulate continuous surface wind field measurements. Temporal continuity allows an estimation of the added value of internal structural changes, and to refine the identification of TC intensity variations and internal dynamics on various time scales. The analyses presented here are thus designed to be applicable to real-time high-resolution observations and potentially included in assimilation datasets. Thus, the main focus is on the properties of the surface wind field that were studied by Vinour et al. (2021).

Based on a set of seven realistic high-resolution simulations, a statistical database synthesizing TC internal structure properties is built. These properties are then related both to the ongoing intensity changes and to internal processes embedded in the rotating-convection paradigm and in the associated symmetric and asymmetric theory. The roles and temporal scales of these parameters are also compared, and their individual and

collective contribution to the statistical prediction of intensity variations are assessed.

The article is organized as follows: the modeling framework, validation data, and studied parameters are described in section 2; we then assess the realism of these simulations, and their statistical representativeness by comparing model outputs to SAR images and best track data in section 3; the temporal changes throughout the TC internal structure are studied in section 4 by relating these changes to TC life cycle in various ways; a final discussion and conclusions are provided in section 5.

2. Datasets and methods

a. The WRF Model configuration

The Weather Research and Forecasting (WRF) Model version 3.7.1 is used in this study with the Advanced Research WRF (ARW) dynamic solver (Skamarock and Klemp 2008). The configurations are designed to model TC inner core on a 1-km horizontal grid. This high resolution is achieved using the vortex-following algorithm provided by WRF with a two-way nesting procedure composed of three domains: a large domain at 9-km resolution encompassing the whole TC track (it is defined as a rectangular box including the track plus 8° on each side) and two vortex-following embedded domains gradually increasing the resolution to 3 and 1 km. The intermediate vortex-following domain is set as an 8° square box around the TC center, and the finer domain as a 4° square box around the TC center. The two nested domains move every 15 min following the TC vortex, thanks to an automatic tracking of low pressure under 50 000 Pa, in a radius determined by a maximum TC translation speed of 40 m s⁻¹. In the moving nests, instead of the default 9-km parent grid topography, high-resolution terrain and land-use files are used to improve the realism of crossed islands and mainlands. On the vertical, all the domains have the same vertical grid composed of 54 terrain-following levels with refinement in the planetary boundary layer (PBL) (ranging from 22-m resolution for the first levels to 60 m at 500 m, and 100 m at 1000-m height), and at the top of the model (set at 5000 Pa). The set of parameterizations used is the following: Betts–Miller–Janjić (BMJ) convective scheme for the 9-km domain, while convection is explicitly solved in the 3- and 1-km nested domains; the Yonsei University (YSU) PBL with revised MM5 Monin–Obukhov surface layer parameterization, the classical Charnock relation for the surface drag coefficient, the WRF single-moment six-class microphysics scheme (WSM-6), the Dudhia shortwave radiation scheme, and the Rapid Radiation Transfer Model (RRTM) for longwave radiation.

Horizontal and vertical resolutions, as well as all parameterization settings are identical for all TC simulations. Initial, surface, and boundary conditions are prescribed with the 0.25° NCEP Final (https://rda.ucar.edu/datasets/ds083.3/) operational global analysis using the Global Data Assimilation System (https://rda.ucar.edu/datasets/ds094.0/). A spectral nudging, using the WRF four-dimensional data assimilation (FDDA) scheme, toward these reanalysis data is also applied during the whole simulations, on the parent 9-km-resolution domain, and above the BL only, with no direct impact on nested domains. The nudging ensures a better consistency of the modeled synoptic flow with observations, limiting the TC track deviations, without constraining the TC physics in the nested domains (Wang et al. 2013). The spectral nudging only applies to large scales of the domain (approximately 1000 km here, i.e., the large domain size divided by 3).

The horizontal resolution of the two inner domains is a compromise between computational cost and a resolution comparable to the SAR images that are resolved at 1 km and resampled (averaged) on a 3-km grid. It should be noted that the effective resolution of the simulations is about 7 km, which is larger than the SAR data resolution of 3 km. The model outputs must thus be considered as smoother than SAR observations. It should also be kept in mind that the TC's intensification as well can be impacted by the effects of numerical resolution (Hasan et al. 2022).

b. SAR observations

SAR observations provide 2D ocean surface wind module products under TCs at a high resolution of 1 km, with a spatial extent of 200–400 km depending on the acquisition mode. In this study, we use a 3-km resampled (averaged) product. SAR is a microwave active sensor, which measures the backscatter signal at C band to estimate the sea surface roughness with a spatial resolution that ranges from 10 m to 1 km (depending on the acquisition mode). The wind field is retrieved using co- and cross-polarization channels with a dedicated inversion algorithm developed by Mouche et al. (2017) to mitigate the signal saturation observed in copolarization (as for scatterometers). Mouche et al. (2017, 2019), and Combot et al. (2020) showed that SAR provides very reliable estimates of TC maximum intensity, and characteristic wind radii. Vinour et al. (2021) showed that they make it possible to measure many properties of the internal TC structure such as the eyewall and near-core surface wind gradients, and inner-core wind azimuthal asymmetries. The database used in this study is the same as the one presented in Vinour et al. (2021). It is composed of 188 images acquired over TCs between 2014 and 2019 by *Sentinel-1A* and *Sentinel-1B*, and *RADARSAT-2* satellites during the Satellite Hurricane Observation Campaign (SHOC) conducted by the European Space Agency (ESA), the Collecte Localisation Satellites (CLS) group, and the French national institute for ocean science (Ifremer). This SAR database statistically represents a wide range of TC events, in all basins and at all categories. It is used here to compare observed and modeled TC internal structure.

c. BT dataset

The International Best Track Archive for Climate Stewardship (IBTrACS; Knapp et al. 2010) combines the best track (BT) data (TC location, maximum wind speed, and characteristic wind radii) from various meteorological centers (regional specialized meteorological centers responsible for TC forecast in the different basins, and government agencies) into a common format. U.S. centers BT data with a 6-h time resolution
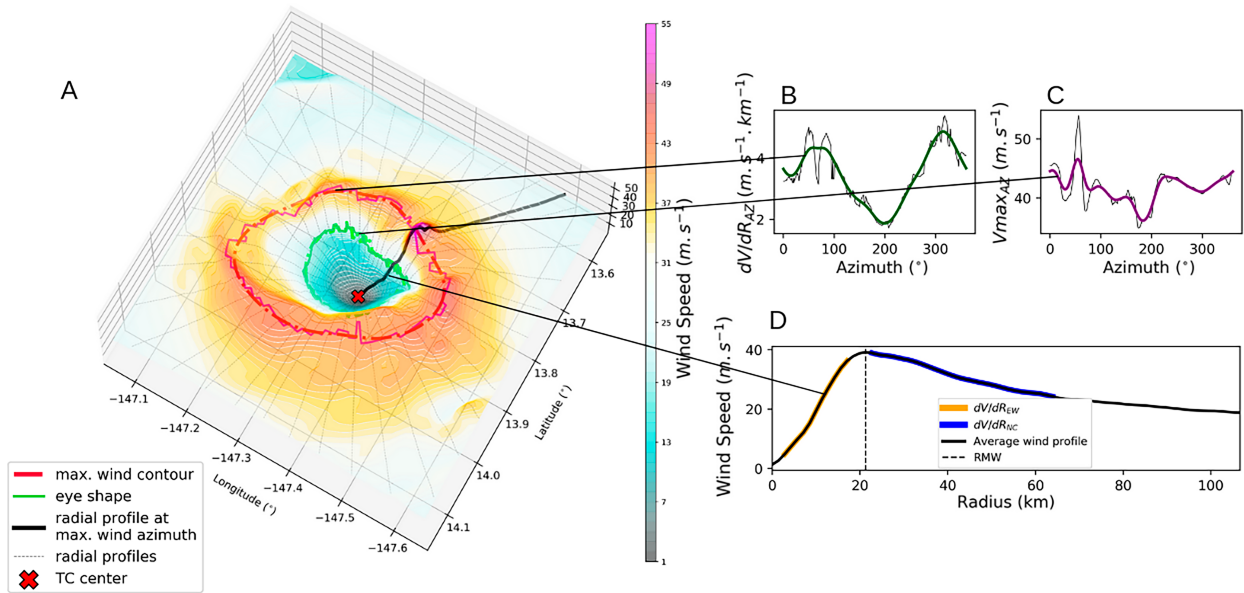
FIG. 1. Illustration of parameters extracted from the surface wind field from an output of the Lane simulation at 0700 UTC 20 Aug 2018. (a) Surface wind field projected on a 3D grid (z axis is wind speed) with distributions of maximum wind (red), maximum eyewall radial gradient (i.e., eye shape, in green), and radial profile (black) superimposed. (b),(c) Raw (thin black) and smoothed (thick) extracted azimuthal distributions of eyewall radial wind gradient and maximum wind, respectively, with the same color code as (a). (d) The extracted radial mean profile and highlighted eyewall (yellow) and near-core (blue) areas.

are used in the present study to assess the representativeness of the simulations in terms of TC characteristics (location, maximum intensity, intensification rate, translation speed).

d. Surface wind field parameters of interest

This study pursues the work of Vinour et al. (2021), who studied the statistical relationships between TC internal structure properties and intensity variations based on SAR snapshots of surface wind speed. Here, we use a dynamical model to simulate the whole TC evolution, this way filling the gap between sparse snapshots. We aim at assessing the characteristic time scales of the different internal properties and the importance of measuring their evolution in time. This would notably provide insights for the potential of having more regular high-resolution surface wind observations such as SAR images, for the research and forecast community. These analyses were thus designed to be applicable to SAR observations and potentially included in real-time assimilation datasets.

The TC internal structure is described from the surface wind speed only, and following the methodology designed by Vinour et al. (2021). This methodology assesses the properties of the 2D surface wind field in a TC-centered relative frame (polar grid with 1-km radial resolution and 1° azimuthal resolution), and extracts radial and azimuthal parameters, which are detailed hereafter and illustrated in Fig. 1.

The radial structure is described by its radial surface wind gradients computed from the azimuthally averaged profile in two characteristic areas: the eyewall area [between the eye and the radius of maximum wind (RMW), yellow in Fig. 1d], and the near-core area (between 1 and 3 times RMW, blue in Fig. 1d). In the eyewall, the radial gradient is also compared

to a Rankine-like vortex (defined as a linear profile between 0 m s^{-1} in the eye and the maximum wind at the RMW) to estimate the eyewall profile sharpness with respect to the RMW. The two obtained gradients are noted dV/dR_{EW} (eyewall) and dV/dR_{NC} (near core); the eye–eyewall sharpness (comparison to Rankine profile) is noted $dV/dR_{EW} - V_{MAX}/RMW$ (cf. Table 1).

The azimuthal structure is described through two variables, for which azimuthal distribution is examined: the eye–eyewall radial wind gradient (dV/dR_{AZ} hereafter, Fig. 1b, Table 1), and the distribution of maximum wind (Vmax$_{AZ}$ hereafter, Fig. 1c, Table 1). Their azimuthal distributions are smoothed with a Butterworth filter with a cutoff frequency corresponding to 40% of the signal explained variance to absorb local anomalies and effects of the polar grid discretization (see, for instance, the effect of smoothing on Vmax$_{AZ}$ in Fig. 1c).

The degree of asymmetry is then quantified through a spectral decomposition of these signals: for each signal, the percentages of explained variance of each WN of the spectral decomposition, from 1 to 180, are computed. They are then gathered into three distinct groups: "low" WNs (WNs 1 and 2) describing the vortex-scale asymmetry induced by large-scale perturbations (i.e., vertical shear) and discrete propagating VRWs (Wang 2002a; Reasor et al. 2009); "medium" WNs (WNs 3–5) associated with smaller-scale processes and characteristic of restoration processes such as eyewall mesovortices (Muramatsu 1986) and the generation of VRWs (Schubert et al. 1999; Kuo et al. 1999); "high" WNs (WNs 6–180) containing the rest of the spectral distribution associated with localized wind anomalies such as convective bursts (Rogers et al. 2013), thus presenting less vortex-scale asymmetry than low and medium WNs. Percentages

TABLE 1. Table summarizing the TC parameters extracted from the simulations, as described in section 2d.

Parameter abbreviation	Brief description
V_{MAX}	Vortex maximum wind intensity: $V_{\text{MAX}} = \max(\text{Vmax}_{\text{AZ}})$
RMW	Radius of maximum wind of the azimuthal-mean wind profile
dV/dR_{EW}	Gradient of the azimuthal-mean wind profile between the flat eye area and the RMW [cf. Vinour et al. (2021) for more details]: $dV/dR_{\text{EW}} = (\Delta \overline{V_r}/\Delta r)_{r_{\min} \to \text{RMW}}$
dV/dR_{NC}	Vortex-averaged near-core radial gradient: $dV/dR_{\text{NC}} = (\Delta \overline{V_r}/\Delta r)_{\text{RMW} \to \text{3RMW}}$
Vmax_{AZ}	Maximum wind intensity at each azimuth
dV/dR_{AZ}	Eyewall wind gradient at each azimuth: $dV/dR_{\text{AZ}}(\theta) = (\Delta \overline{V_{r_\theta}}/\Delta r_\theta)_{r_{\theta\min} \to r_{\theta\max}}$
$\text{Var}_{k_1 - k_2}(S_{\text{AZ}})$	Percentage of variance explained by WNs k_1 to k_2 from the spectral decomposition of azimuthal signal S_{AZ}
$\text{WNT}(S_{\text{AZ}})$	Wavenumber trend of azimuthal signal S_{AZ} [cf. definition (1)]

of explained variance for each group are hereafter noted Var_{1-2}, Var_{3-5}, and Var_{6-180}. Note that the results hereafter are not strongly sensitive to the range of WNs picked to define the groups (e.g., we could have taken WN1, WN1–2 or WN1–4 for low WNs, and WN3–180 or WN6–180 for high WNs, and keep the same qualitative results). The choice of groups was thus made to optimize the characterization of the asymmetry distribution (cf. definition of temporal variables in section 2e), as well as for better consistency with asymmetric processes described in the literature.

The radial and azimuthal descriptors are estimated at each hourly model output for all simulations.

e. Estimation of inner-core temporal changes

Three variables are considered to describe the TC intensity variations: the maximum intensity (V_{MAX}), its first time derivative [i.e., intensification rate, hereafter noted $\partial_t(V_{\text{MAX}})$], and its second time derivative [i.e., increase or decrease of intensification rate, hereafter noted $\partial_t^2(V_{\text{MAX}})$]. Their extrema are used to describe specific phases of the TC life cycle such as intensity peaks and troughs, strongest intensifications and strongest weakenings, or intensity restorations (i.e., increasing rate) and deteriorations (i.e., weakening rate).

To assess the evolution of the TC internal structure in regard to these TC life cycle changes, time derivatives of the radial and azimuthal descriptors are evaluated. An additional metric called "wave number trend" (WNT hereafter) is also designed to measure the time evolution of the asymmetry distribution among scales around the vortex. It is computed as the difference in wind variance growth/decay between two sets of scales, the high and low WN groups defined in the previous section:

$$\text{WNT}(S_{\text{AZ}}) = \partial_t[\text{Var}_{6-180}(S_{\text{AZ}})] - \partial_t[\text{Var}_{1-2}(S_{\text{AZ}})], \quad (1)$$

where $\partial_t[\text{Var}_{1-2}(S_{\text{AZ}})]$ and $\partial_t[\text{Var}_{6-180}(S_{\text{AZ}})]$ denote the time derivatives of the smoothed time series of explained variance by low and high wavenumbers (Var_{1-2} and Var_{6-180}) for a given signal S_{AZ}. Note that WNTs are not defined if the two time derivatives of low and high WNs are of the same sign, but only if the trends of high WNs and low WNs are opposed. The WNT is thus positive when the variance explained by high WNs is increasing, while that explained by low WNs is

concurrently decreasing. In such cases, the wind field asymmetry increases at small scales; it is more localized and widespread in azimuth. When the trend is negative, the variance increases in low WNs and is associated to a more polarized wind field with concentration of the asymmetry in vortex-scale patches. The polarized regime, generally related to synoptic shear events, was associated in previous studies with a deterioration of TC intensity (Frank and Ritchie 2001; Reasor et al. 2004), while the spreading and distribution of asymmetry in azimuth to the generation of convective bursts and the promotion of intensification (Guimond et al. 2016a; Hazelton et al. 2017). The WNT metric thus tends to diagnose the evolution of the TC structure toward reinforcement (thus rehomogenization/symmetrization) or decay (generally increased asymmetry with decay). Medium WNs (3–5) are deliberately not considered here, as interpreted in the observational study of Vinour et al. (2021) as a transient phase of perturbation traducing a spontaneous response of the eyewall to externally induced disruptions (through generation of eyewall mesovortices for instance).

A smoothing of the time series is performed to consider only persistent variations of the parameters of interest, and ignore short localized variations. The effect of smoothing on V_{MAX} and azimuthal variances is shown in Fig. 2. As can be inferred, the variability of raw time series can be very large (cf. thin black lines in Figs. 2a,b), preventing the extraction of life cycle phases or computation of meaningful time derivatives. The smoothing was thus chosen to absorb the high time variability, while being representative of intensity changes (peaks, troughs, increase, or decrease in intensification rates). The smoothing is applied using a Butterworth filter with a cutoff period of 12 h. This cutoff period is the default one used for most analyses, but larger periods were also tested in section 4d to isolate even longer-scale changes. All time derivatives are computed over the smoothed signals, allowing a better identification of intensity variations (see triangle markers in Fig. 2a). The smoothing also makes it possible to extract consistent phases of negative and positive WNTs, such as those highlighted by the green and red rectangle, that go with changes in $\text{Var}_{1-2}(\text{Vmax}_{\text{AZ}})$ and $\text{Var}_{6-180}(\text{Vmax}_{\text{AZ}})$ that are barely visible on raw signals.

The various notations and abbreviations introduced above and used in the following sections are summarized in Table 1.
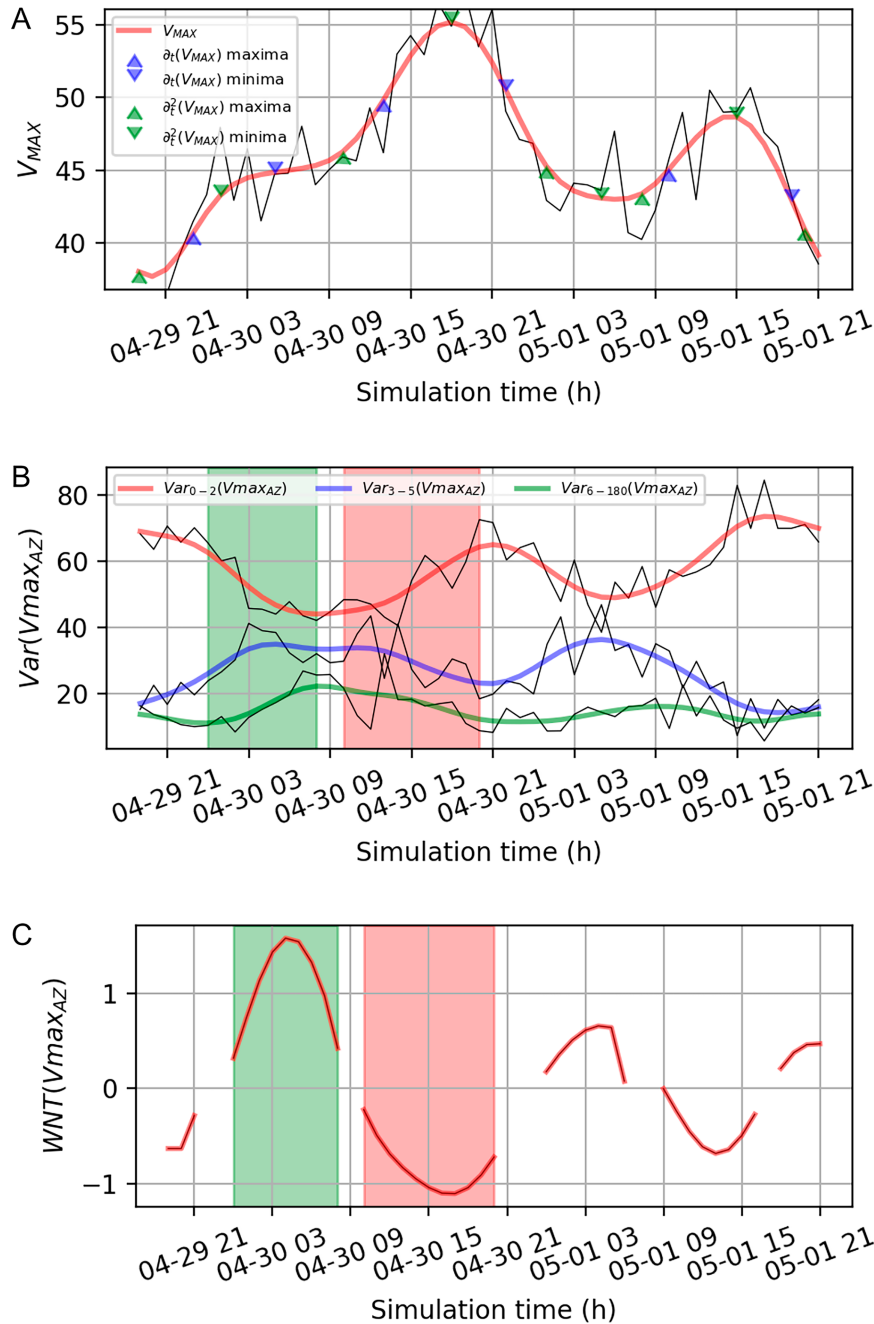
FIG. 2. Illustration of temporal changes estimations on the simulation of TC Fani. (a) Intensity raw time series (thin black line) and smoothed with a 12-h cutoff period Butterworth filter (thick red), along with extracted local minima and maxima of $\partial_t(V_{MAX})$ and $\partial_t^2(V_{MAX})$ computed from the smoothed curve denoted by red and blue triangles. (b) Time series of smoothed $Var_{1-2}(Vmax_{AZ})$ (red), $Var_{3-5}(Vmax_{AZ})$ (blue), and $Var_{6-180}(Vmax_{AZ})$ (green) computed from raw signals (thin black curves). (c) Time series of $WNT(Vmax_{AZ})$ computed from $\partial_t[Var_{1-2}(Vmax_{AZ})]$ and $\partial_t[Var_{6-180}(Vmax_{AZ})]$. The maximum positive and minimum negative phases of $WNT(Vmax_{AZ})$ are highlighted in green and red shadings in (b) and (c).

TABLE 2. Summary of WRF simulated events and domain extents.

Event name	Start date–end date	Basin	Category (WRF)	Category (obs)	Outer domain extent
Irma	31 Aug–11 Sep 2017	Northern Atlantic	4	5	8.3°–35.5°N, 99.9°–24.1°W
Cebile	27 Jan–4 Feb 2018	Southern Indian	5	4	29.9°–4.1°S, 67.6°–92.5°E
Lane	16–24 Aug 2018	Eastern Pacific	5	5	2.7°–27.0°N, 166.0°–120.5°W
Mangkhut	8–16 Sep 2018	Western Pacific	4	5	5.7°–30.3°N, 102.7°–164.1°E
Trami	22–30 Sep 2018	Western Pacific	4	4	8.9°–43.7°N, 118.7°–146.0°E
Joaninha	23–30 Mar 2019	Southern Indian	5	4	32.8°–8.7°S, 53.6°–77.4°E
Fani	29 Apr–3 May 2019	Northern Indian	3	4	2.7°–27.6°N, 75.9°–95.1°E

f. Classification

A machine learning classification method is used to assess the predictive potential of the extracted TC descriptors. The objective is to evaluate if these descriptors provide significant information to dissociate the TC life cycle phases. The classification here focuses on dissociating positive and negative values of $\partial_t(V_{MAX})$ (i.e., intensifications and weakenings), with classes defined under the 1/3 and above the 2/3 quantiles of their distribution.

We follow the classification method developed in Vinour et al. (2021), which is adapted to a dataset with a limited amount of samples and a large number of variables describing the dataset. Here, in order to limit the overfitting between correlated consecutive time steps, the number of samples is equal to one-fourth of the total number of outputs (i.e., one sample every 4 h of simulation) minus a random one-tenth of the remaining samples (this step is reproduced 10 times using a bootstrap method), which yields 233 samples per classification. The number of variables considered for the classification is 12: three vortex-scale parameters (maximum wind, RMW, and latitude), two instantaneous mean profile parameters (dV/dR_{EW} and dV/dR_{NC}) and their two time derivatives, two instantaneous azimuthal parameters describing high WN variance in amplitude variability [$Var_{6-180}(dV/dR_{AZ})$ and $Var_{6-180}(Vmax_{AZ})$] and the corresponding temporal WNTs [$WNT(dV/dR_{AZ})$ and $WNT(Vmax_{AZ})$], and one random control variable. The classification is performed over 495 random combinations of four variables among the 12 aforementioned, and with 10 machine learning models (this makes it possible to account for a wide range of dependences between variables, including nonlinear ones, as well as to get rid of issues and specific biases associated with each classification model). The average score of the 10 models is computed for each combination. Studying the composition of the best combinations then makes it possible to identify the most decisive variables in the dissociation of intensification phases.

A sensitivity analysis of the classification results to the time smoothing of signals is performed. Classifications with descriptors computed from signals smoothed with 12-, 24-, and 48-h cutoff periods are compared.

3. Modeled cases and validation

a. Description of simulations

Seven distinct events were simulated, in various basins, and with various characteristics: Irma (2017, North Atlantic),

Cebile (2018, south Indian), Lane (2018, northeast Pacific), Mangkhut (2018, northwest Pacific), Trami (2018, northwest Pacific), Joaninha (2019, south Indian), and Fani (2019, north Indian).

They are detailed in Table 2 and Fig. 3, along with the geographic extent of the model parent domain. These simulations were chosen to describe major TCs (categories 4 and 5) in different basins, and with a wide range of life cycle evolutions including several intensity changes during their mature phases. In addition, TCs with few interactions with land were preferred, as they make it possible to witness scale interactions, and gradual internal changes instead of disturbances caused by external constraints. These simulations were not designed to reproduce the most realistic TCs, but to provide a sufficiently diverse database to study the inner-core structural changes in relation to the TC intensity changes during the mature phase of the TC life cycle.

Figure 3 shows the seven modeled TC tracks and V_{MAX} time series. All tracks match well the BT data, as spectral nudging applied on the large domain ensures synoptic dynamics close to observations. Simulated maximum wind, on the other hand, can be quite different from BT data. The maximum reached intensity is underestimated for Irma, Mangkhut, Trami, and Lane, and overestimated for Cebile, while Fani does not maintain its intensity before landfall, and Joaninha does not capture the maximum intensity peak although matching the first intensification. Time steps above category 4 are rare; this can be due to a bias induced by the resolution (horizontal and vertical), which may be still too coarse to properly solve these very intense and contracted phases, or to the model numerics [notably implicit numerical dissipation as suggested by Guimond et al. (2016b) and Hasan et al. (2022)], or parameterizations, notably the microphysics, surface, and boundary layer parameterizations (Nolan et al. 2009b; Li and Pu 2008). The maximum wind time series also reveal some lagged or missed changes in intensity, or similar changes but of lower intensity (e.g., for Lane). Such discrepancies were however expected. They arise from several reasons: 1) the model biases (resolution, numerics, parameterizations) that can lead to misrepresented physical processes, 2) the stochastic nature of the Navier–Stokes equations. However, all simulated TCs intensify to mature TCs, and all of them feature either long mature phases with short-range intensity fluctuations around the peak intensity (Irma and Cebile), or notable weakenings and reintensifications with secondary intensity peaks (Trami, Mangkhut, Fani, Lane, Joaninha). The diversity of cases and external conditions makes it possible to have
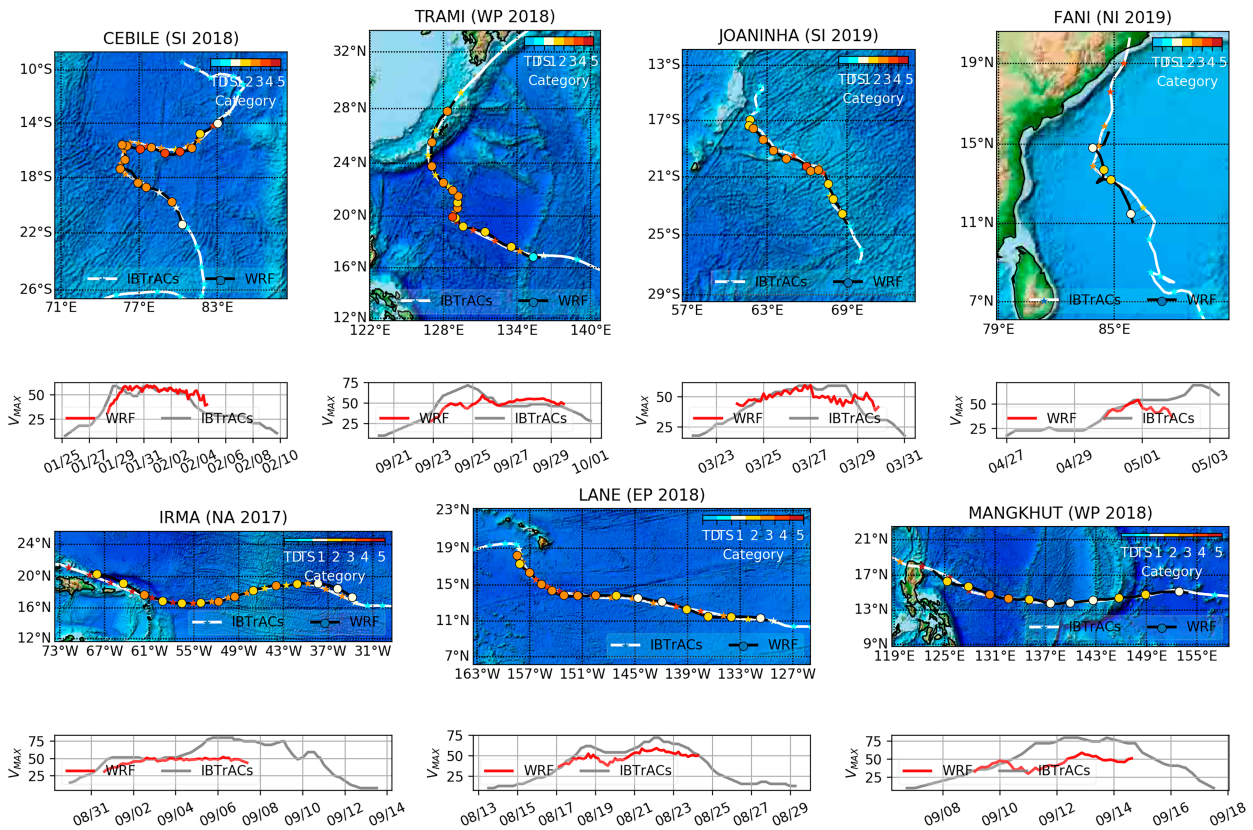
FIG. 3. Summary of WRF simulated tracks (maps) and intensity (V_{MAX}) times series (line plots) for the seven simulations compared to IBTrACS. WRF simulations are denoted by black tracks and circle markers in the map panels, and red curves on V_{MAX} comparisons; IBTrACS data are denoted by white tracks and cross markers, and gray curves on V_{MAX} plots. Marker color in the map panels indicates the category based on the Saffir–Simpson scale.

TCs with notable intensity changes and a significant variability in the mature TC life cycle description, which was the design of this study. In addition, Fig. 4 statistically compares some TC parameters of the simulations [i.e., (Fig. 4a) V_{MAX}, (Fig. 4b) absolute latitude, (Fig. 4c) translation speed, and (Fig. 4d) intensification rate $\partial_t(V_{MAX})$] to those of SAR and BT databases. Overall, the distributions are comparable in terms of variability. The normalized distribution of maximum wind is centered around 55 m s^{-1}, the latitude distribution centered around 15°, and the translation speed around 5 m s^{-1}, indicating the bias due to the choice of studying mature TCs. The intensification rate distribution is moreover very well represented, indicating the consistency of simulated TC life cycle dynamics.

The statistical validation of these simulations and extracted parameters of interest against SAR observations is further detailed in the next section.

b. Statistical validation against SAR

The radial and azimuthal parameters describing the TC surface wind field in the present study are validated against SAR observations.

The distributions of the inner-core and near-core radial gradients shown in Figs. 5a and 5b shows that the model misses the strongest radial gradients. The azimuthal variances of

eyewall gradient (Fig. 5c), and maximum wind ring (Fig. 5d) azimuthal variances are shifted toward slightly lower values than SAR observations indicating an underestimation of their variability. But overall, modeled distributions are satisfactorily close enough to observations.

The model ability to represent inner-core observed TC structure is further illustrated with the relation between RMW and maximum wind illustrated in Fig. 6. This relation is a good way to get a first view of the TC dynamics, as the TC vortex is expected to contract inward when intensifying under the effect of gradient wind balance and angular momentum conservation. This relation was clearly observed in SAR observations (Vinour et al. 2021), and is represented in black in Fig. 6. The simulations also show a decrease of RMW with V_{MAX}, but at a weaker rate, with a median value of 40 km for tropical storms (compared to 50 km in SAR data), and 25 km for category 4 TCs (compared to about 18 km in SAR data). Here again, the highest intensities appear as probably less well resolved in the model due to resolution issues. On another hand, the limit in statistical representativeness of the seven cases is also visible, as the individual simulations can impact the median values for a given category: for instance, the high values of RMW in category 3 are mostly all attributable to Trami (light green dots), which kept a strong intensity while it reached relatively high latitudes, and therefore
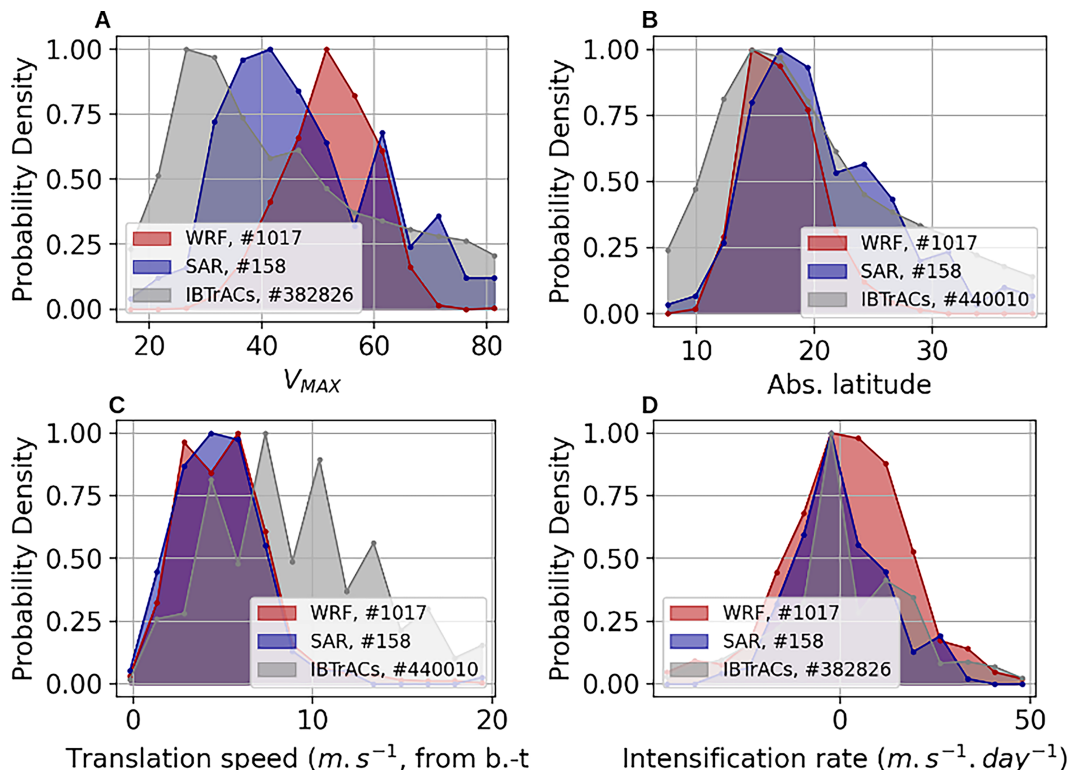
FIG. 4. Comparison of normalized histograms between WRF (red; 1017 samples), SAR (blue; 158 samples), and IBTrACS (382 826 minimum samples) showing distributions of (a) V_{MAX}, (b) absolute latitude, (c) translation speed, and (d) $\partial_t(V_{\mathrm{MAX}})$. Time-dependent variables in (c) and (d) are estimated from IBTrACS for the SAR distribution.

dilated in size. However, the range of TC simulations overall makes it possible to feature the average TC eye contraction.

The properties of the mean radial wind profile of simulated TCs are also compared to the SAR distributions studied in Vinour et al. (2021), and shown in Fig. 7. The composite radial profiles by TC intensity category (Fig. 7a) show a fair agreement between WRF and SAR for categories 0–3, while category 4 is significantly underestimated in WRF, and category 5 is not represented (the average of the radial profile put the few category 5 outputs in an average category 4 profile). It is however notable that WRF profiles are slightly more intense (by approximately 2 m s^{-1}) on average than SAR ones for categories 1, 2, and 3. This slight difference is explained by the higher modeled median values in each category (see the x location of the medians in Fig. 6), as well as by a lower azimuthal standard deviation of the maximum wind contour (standard deviations by category are indicated in the legend of Fig. 7; average over all categories is 3.28 for WRF and 4.10 for SAR) likely due to the WRF effective resolution (about 7 km) that results in a slightly smoother wind distribution compared to SAR (3-km effective resolution).

Looking at the eyewall gradient sharpness, TC simulations are shown to slightly depart from the Rankine-like profile (Fig. 7b), but much less than SAR observations for TC intensities above category 3. Similarly, the near-core area (Fig. 7c) shows a smoother profile than SAR observations for TC outputs of categories 4 and 5. This indicates a

limit in the model ability to resolve sharp wind gradient due to its resolution and to numerics and parameterization induced biases.

4. Links between the TC life cycle and its internal structural evolution

a. Time scales

The TC life cycle variations are characterized with 3 time series: the TC intensity (V_{MAX}), its time derivative [intensification rate, $\partial_t(V_{\mathrm{MAX}})$], and its time second derivative [variations of intensification rate, $\partial_t^2(V_{\mathrm{MAX}})$]. As shown by the normalized temporal spectra of these signals (Fig. 8a), the 3 time series describe the life cycle evolution at various scales with peak periods of, respectively, 107, 23, and 18 h. The 107-h average peak period for intensity corresponds to the average duration of simulations, showing that the largest variability is basically associated with the intensification and decaying phases over the whole life cycle time scale, with relatively low energy under 24-h period. On the other hand, its derivatives have a signal concentrated between 30- and 12-h peak periods, related to shorter variations of daily or half-daily time scales.

The parameters extracted to describe the TC surface wind field structure (radial gradients, azimuthal variances, wavenumber variances, and WNTs) are also found to vary at different time scales; dV/dR_{EW} and dV/dR_{NC} evolve on
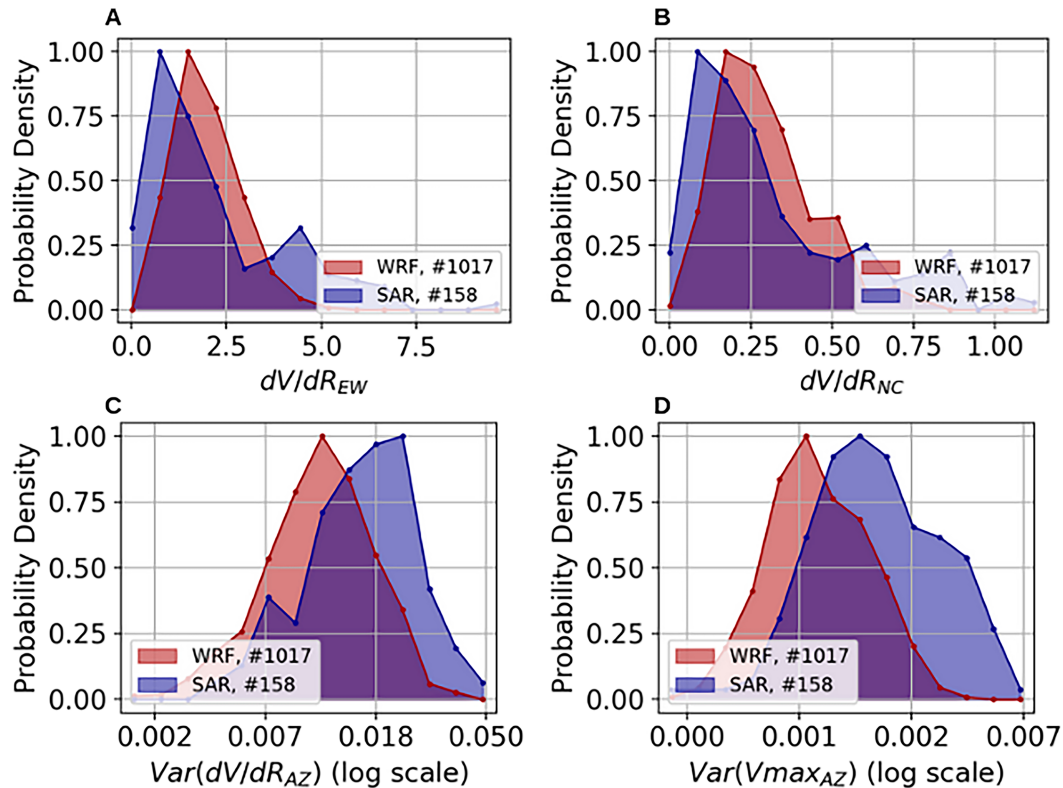
FIG. 5. Comparison of histograms between WRF (red; 1017 samples) and SAR (blue; 158 samples) showing distributions of (a) dV/dR_{EW}, (b) dV/dR_{NC}, (c) Var(dV/dR_{AZ}), and (d) Var(Vmax$_{\text{AZ}}$).

characteristic time periods slightly lower than intensity (most energy between 107 and 12 h, with peak periods of 107 h; see Fig. 8b). This is in agreement with the relation found between intensity and radial gradient observed in Fig. 7. The estimation of the curvature of the eyewall profile ($dV/dR_{\text{EW}} - V_{\text{MAX}}/\text{RMW}$) shows a broader spectrum toward smaller scales, with a peak period of 66 h. It is indeed the radial parameter most related to smaller scales, notably to eyewall mixing (Kossin and Eastin 2001; Nguyen et al. 2011; Vinour et al. 2021). Variance explained by low and high wavenumbers of dV/dR_{AZ} and Vmax$_{\text{AZ}}$ (Figs. 8c,d) also peaks at large time scales (107 h) but with a broader spectrum than intensity and radial gradients and a marked secondary peak around 24 h. The variance of middle wavenumbers shows the largest peak at 24 h and largest density of spectrum at low periods between the three WN groups, indicating their more transient character. Finally, the WNTs within these azimuthal signals are found to evolve on the shortest time scales, with a spectrum centered around 22 h close to the time scales of $\partial_t(V_{\text{MAX}})$ and $\partial_t^2(V_{\text{MAX}})$ for Vmax$_{\text{AZ}}$, and even lower peak period of 10 h for dV/dR_{AZ}, which also indicates the more transient character of eye–eyewall asymmetric variations compared to the maximum wind ring. This first assessment thus shows that radial gradient are more related to the life cycle scale of intensity variations, while the azimuthal asymmetry and WNTs are more related to shorter intensity variations, notably changes in the intensification rate.

b. Case studies

To further understand the link between the internal TC structure descriptors and the TC evolution, a few case studies are first examined. The time series of dV/dR_{NC}, $dV/dR_{\text{EW}} - V_{\text{MAX}}/\text{RMW}$, Var$_{1-2}$(Vmax$_{\text{AZ}}$), and Var$_{6-180}$(Vmax$_{\text{AZ}}$) superimposed with the V_{MAX} time series during the Lane simulation are shown in Fig. 9.

For this TC case, the correlation between TC intensity and radial gradients time series is strong (0.9 cross correlation with dV/dR_{NC}, 0.63 with $dV/dR_{\text{EW}} - V_{\text{MAX}}/\text{RMW}$, Figs. 9a,b). The near-core radial profile follows the evolution of intensity (higher intensity goes with sharper wind profile, cf. Fig. 9a and Fig. 9b). On the other hand, the correlation between azimuthal variances and life cycle evolution is lower [-0.45 cross correlation with Var$_{1-2}$(Vmax$_{\text{AZ}}$), 0.52 with Var$_{6-180}$(Vmax$_{\text{AZ}}$), Figs. 9c,d]. Azimuthal variances also have a higher variability than the dV/dR_{NC} signal, but a consistent shift between low and high wavenumbers is observed in conjunction with intensity changes: the increase in intensity toward V_{MAX} peak goes with a higher explained variance in WNs 6–180 (Fig. 9d), which is with a more homogeneous distribution of winds around the vortex, and a concurrent decrease in WNs 1–2 explained variance (Fig. 9c).

The link between WNTs and intensity is further assessed during specific phases of TCs Lane and Fani, displayed in Fig. 10. For each simulation, the phases of maximum positive
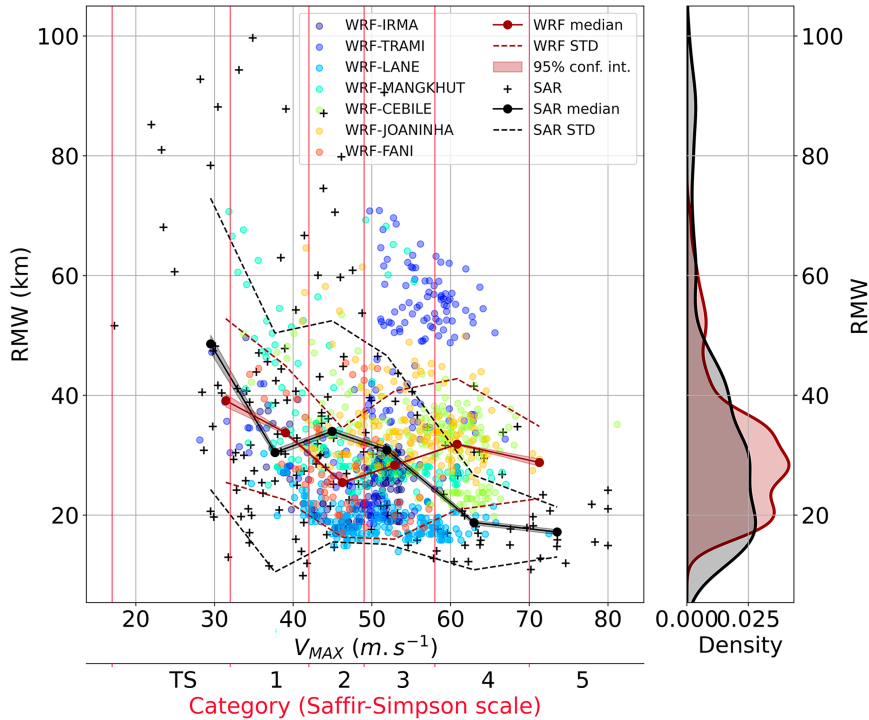
FIG. 6. (a) Comparison of RMW distributions and binned values by category with respect to V_{MAX} between SAR and WRF simulations. SAR samples are denoted by black crosses. WRF samples are denoted by small dots colored according to the simulated event. Binned median values are shown as blue (SAR) and red (WRF) dots with shading showing the bootstrap distribution. Upper and lower distribution quartiles are shown by dashed lines. (b) WRF (red) and SAR (blue) PDF distributions of RMW values.

WNT (i.e., spectral distribution shifting toward high wavenumbers) and minimum negative WNT (i.e., from high to low wavenumbers) are highlighted (green and red shaded areas, respectively), and snapshots of the modeled 10-m wind speed at the beginning and ending of these phases are shown. The Fani simulation (Fig. 10a) shows a clear alternation between positive and negative WNT(Vmax$_{\mathrm{AZ}}$): positive trends occur before or during phases of reintensification, and negative trends before and during intensity peaks, i.e., when intensification weakens. The time lag between WNT(Vmax$_{\mathrm{AZ}}$) and V_{MAX} is slightly negative: the phase opposition of WNT(Vmax$_{\mathrm{AZ}}$) is shifted to the left of approximately 3 h.
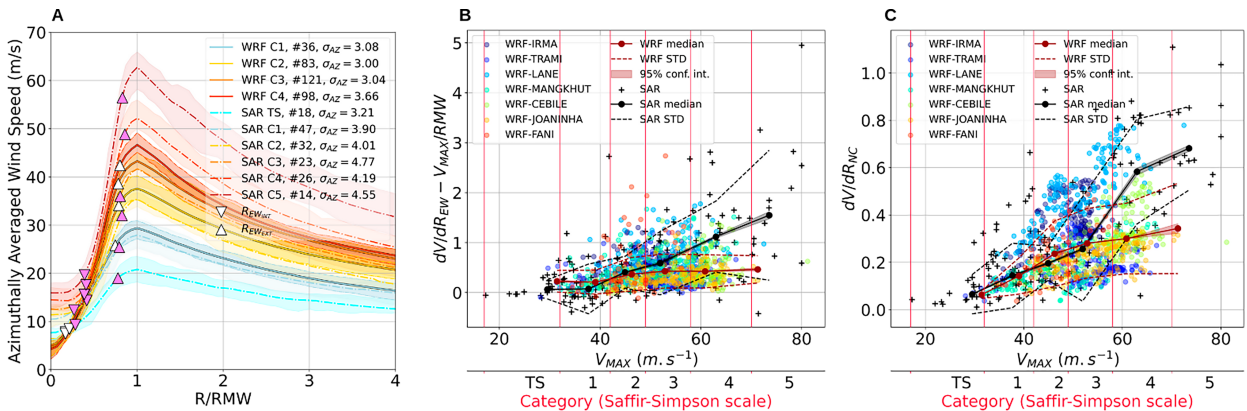

FIG. 7. (a) Comparison of WRF (solid) and SAR (dashed) mean radial profiles composited by intensity category, with shadings denoting the quartiles of each category. Upper and lower triangle markers show the positions of outer and inner limits of the eyewall maximum gradient area, respectively, delimited by maximum and minimum values of curvature for WRF (white) and SAR (purple). The number of samples by category (#) and the average standard deviation of the azimuthal maximum wind distribution for each category (σ_{AZ}) is provided in the legend. (b),(c) As in Fig. 6a, but for the distributions of $dV/dR_{\mathrm{EW}} - V_{\mathrm{MAX}}/\mathrm{RMW}$ and dV/dR_{NC}.
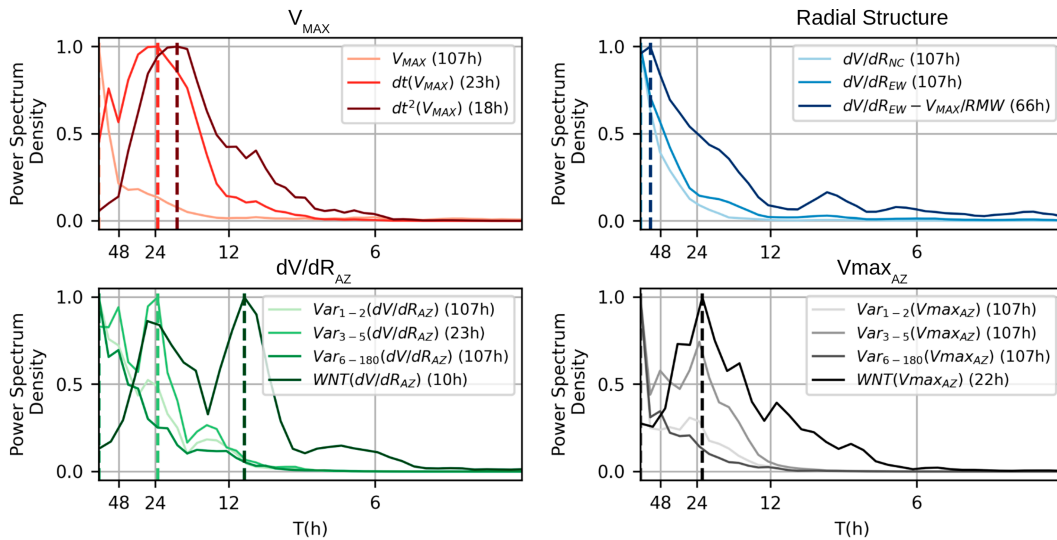
FIG. 8. Normalized power spectra of WRF-extracted time series as a function of period in hours, with peak periods denoted by dashed vertical lines. (a) Intensity variations descriptors: V_{MAX} (light), $\partial_t(V_{MAX})$ (medium), and $\partial_t^2(V_{MAX})$ (dark). (b) Radial profile descriptors: dV/dR_{NC}, dV/dR_{EW}, and $dV/dR_{EW} - V_{MAX}/RMW$. (c) Eyewall radial gradient azimuthal descriptors: $\text{Var}_{1-2}(dV/dR_{AZ})$, $\text{Var}_{3-5}(dV/dR_{AZ})$, $\text{Var}_{6-180}(dV/dR_{AZ})$, and $\text{WNT}(dV/dR_{AZ})$. (d) As in (c), but for Vmax_{AZ}.

Focusing on the two highlighted phases (green and red shading), the first positive trend starts approximately 10 h before the beginning of the reintensification, and is characterized by a contraction, intensification, and symmetrization of the wind field as indicated by the two left snapshots in Fig. 10a. Although there is still a wavenumber-1 asymmetry with stronger winds on the eastern side of the vortex on the second snapshot, it is clear that the maximum wind distribution is much more widespread and homogeneous in azimuth inside the eyewall. The negative trend also starts about 10 h before the intensity peak, during the intensification that follows the previous positive trend. This time, the two snapshots (right side of Fig. 10a) show a strong growth of the asymmetry degree: while at the beginning of the phase the

eyewall has a triangular shape with little variations in the maximum wind distribution except in some areas (such as north and southeast of the eyewall) that might denote the presence of eyewall mesovortices enhancing the wind speed, the second snapshot shows an elliptical eyewall with much stronger winds in the southern half of the vortex. The perturbation of the wind field and growth of asymmetry (which seems to be linked to eyewall mesovortices and polygonal eyewall at the beginning) thus lead to a strongly asymmetric wind field, going with the beginning of intensity decay. All other local maxima and minima of WNTs are also nearly synchronized with the phases of intensity restoration (WNT trough) or deterioration (WNT peak).
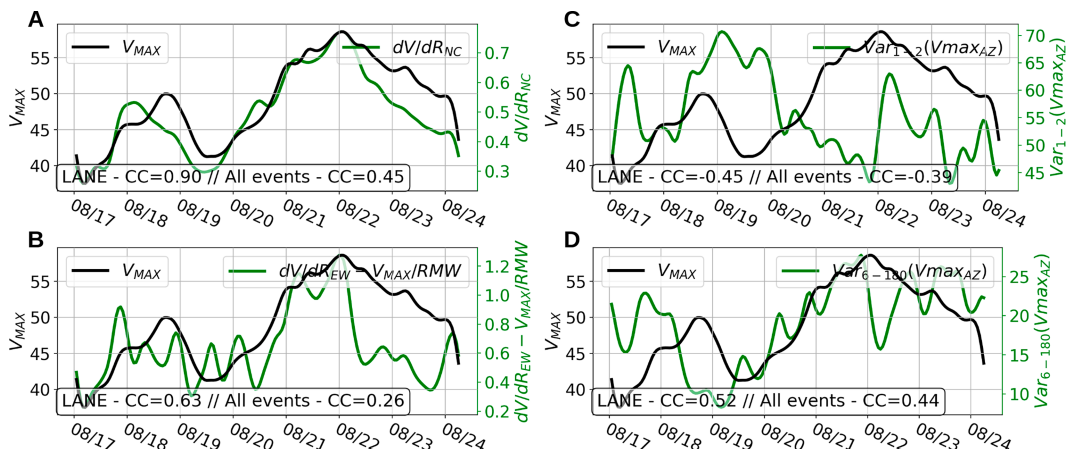

FIG. 9. Time series of (a) dV/dR_{NC}, (b) $dV/dR_{EW} - V_{MAX}/RMW$, (c) $\text{Var}_{1-2}(\text{Vmax}_{AZ})$, and (d) $\text{Var}_{6-180}(\text{Vmax}_{AZ})$ (green curves) superimposed with the V_{MAX} time series (black curves) during the Lane simulation. Text boxes indicate the cross correlation (CC) between the two plotted variables on the Lane simulation alone (i.e., plotted curves) and averaged over all seven TC simulations.
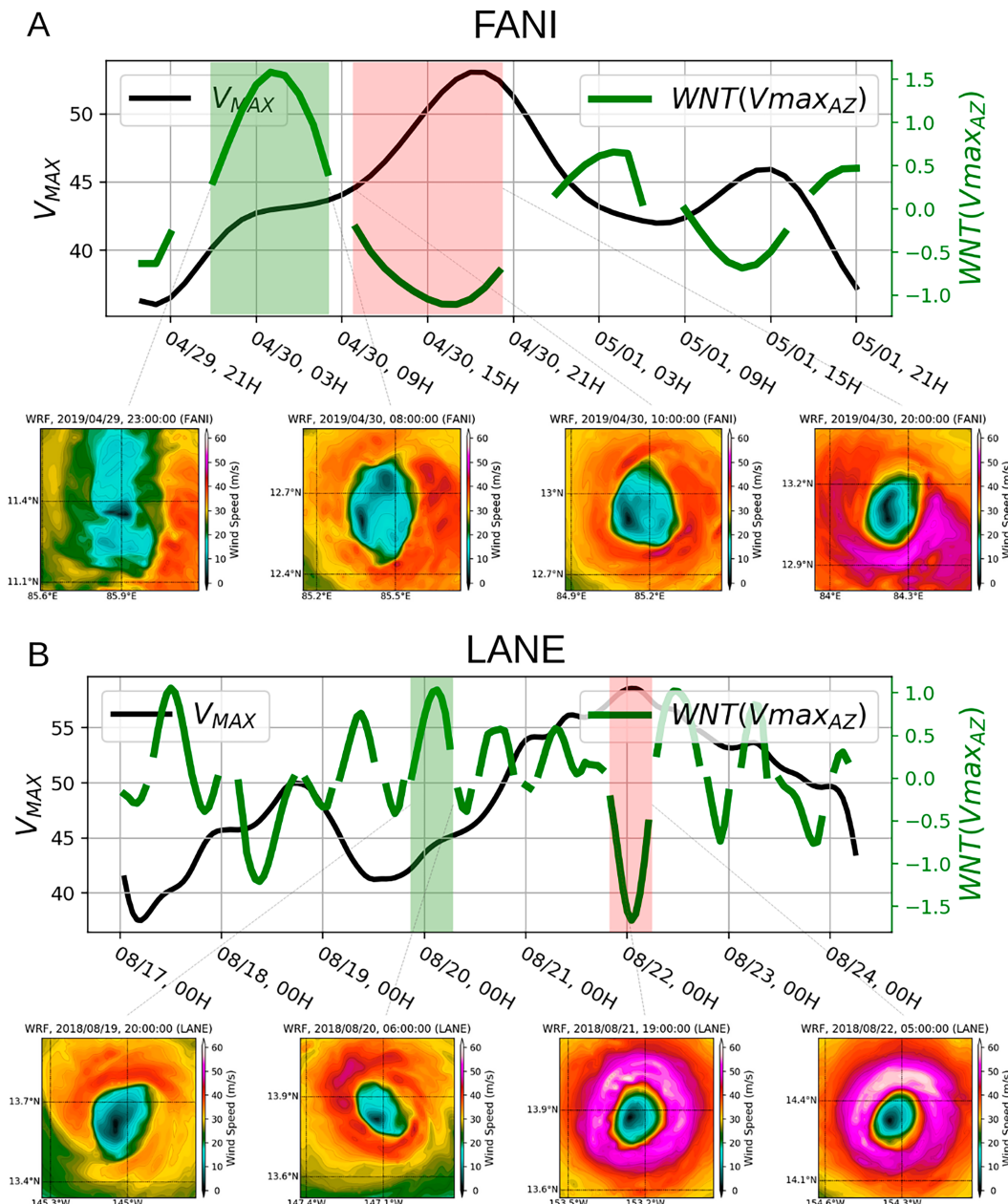
FIG. 10. Superimposed time series of V_{MAX} (black curves) and WNT($Vmax_{AZ}$) (green curves) for simulations of (a) Fani and (b) Lane. The strongest phase of positive trend is denoted by green shading for each simulation and the strongest negative trend by red shading. For each of these intense WNT phases, snapshots of the surface wind field at the initial and final time steps of the WNT event are displayed.

The evolution of Lane shown in Fig. 10b is more complex, as it is much longer with shorter and more numerous reintensification and weakening phases. However, the two highlighted phases show similar features than for the Fani life cycle. The maximum of positive WNT($Vmax_{AZ}$) on 20 August is observed prior to a marked reintensification: approximately four hours after the end of the positive trend phase, the TC undergoes a phase of rapid intensification. Judging by the corresponding snapshots (two left images in Fig. 10b), it appears

that the TC recovers from an eyewall breaking event: the first snapshot shows a discontinuous maximum wind contour with a partially broken eyewall in the southwest corner, while the second snapshot shows a reformed maximum wind ring. It is thus likely that the decrease in intensification that occurs shortly before 20 August was associated with an eyewall breaking event and disturbance of the maximum wind ring, which was then quickly counteracted by an axisymmetrization process. This process then allowed the TC to intensify much

TABLE 3. Best average lagged cross correlations between time series of internal parameters and maximum wind V_{MAX} along with corresponding best lag. Cumulative sums of WNTs are computed, as WNTs alone are temporal derivatives and thus have a low correlation with V_{MAX}.

Internal parameter	dV/dR_{NC}	dV/dR_{EW}	$dV/dR_{EW} - V_{MAX}/RMW$	Cumulative sum [WNT(dV/dR_{AZ})]	Cumulative sum [WNT(Vmax$_{AZ}$)]
Best cross correlation with V_{MAX}	0.472	0.451	0.381	0.390	0.677
Best lag (h)	−4	−4	−4	−20	−6

faster with a restored symmetry in less than 12 h. The minimum of negative WNT(Vmax$_{AZ}$) is in turn simultaneous with the maximum intensity peak on 22 August, at the beginning of the weakening phase. As for the positive trend, this strong negative trend is associated with a notable change in the TC structure, as shown by the two snapshots on the right side of Fig. 10b, the wind field which is quite symmetric with local isolated maxima on 21 August becomes asymmetric with a wavenumber-1 marked maximum on the northern part of the vortex on 22 August.

These two case studies thus show that marked changes in the maximum wind distribution are related to intensity changes, although the time lag can vary significantly in each situation. Moreover, it appears from the Lane life cycle that, when intensity variations are numerous and on small time scales, the relation is less evident. Thus, although pattern emerges from these specific cases, a clear correlation seems difficult to obtain.

c. Composites and statistical behaviors

Previous case studies have shown that WNTs generally features a phase lag with intensity variations. To further generalize and identify statistically robust behaviors, a lag-sensitive study of the average cross correlations of each structural variable with TC intensity is performed over the seven case studies. The largest correlation and its corresponding lag for each internal (radial and azimuthal) parameter is given in Table 3. For WNTs, the cumulative sum of WNTs is computed as it is based on time derivatives and hence correlated to V_{MAX} time derivative rather than its amplitude. The best correlation is observed for WNT in the maximum wind contour, WNT(Vmax$_{AZ}$) (67.7% on average over all simulations), with a negative lag of 6 h. Near-core and eyewall gradients, dV/dR_{NC} and dV/dR_{EW}, show correlation with intensity of 47.2% and 45.1%, respectively, with lags of −4 h (i.e., slight anticipation). WNT of the eye–eyewall gradient, WNT(dV/dR_{AZ}), shows lower correlations (39.0%) with a large negative lag, indicating that its connection to V_{MAX} is hardly detectable on average over all simulations. The cumulative sum of WNT(Vmax$_{AZ}$) thus appears on average more correlated to intensity than radial parameters, indicating that the symmetry (as cumulated WNTs quantify the azimuthal spectrum broadness) of the maximum wind ring anticipates intensity changes.

To refine the statistical identification of intensity variations, composite analyses during phases of strong intensity variations are studied. First, phases of RI (>15 m s^{-1} day^{-1}) and rapid weakening (RW; <-15 m s^{-1} day^{-1}) are examined (Fig. 11). The radial wind gradients time derivatives are

positive during RI phases (Fig. 11a), and negative during RW phases (Fig. 11c) with a slight lag of −2 to 1 h for their extremes. On the other hand, the azimuthal WNTs are positive on average before and at the beginning of RI phases (Fig. 11b), and negative before and at the beginning of RW phases (Fig. 11d). WNT(Vmax$_{AZ}$) shows stronger values than WNT(Vmax$_{AZ}$), and a marked lag of about −5 h.

Cases of restoration and deterioration of intensification were also studied (Fig. 12). Radial gradients tend to increase during restorations and decrease during rapid deteriorations. WNT(Vmax$_{AZ}$) evolves similarly but with a slight anticipation and more marked variations (Figs. 12b,d, green curve), especially during deterioration phases where the composited WNT(Vmax$_{AZ}$) peaks $\Delta_t = 1$ h while all radial parameters still decrease steadily up to $\Delta_t = +4$ h. On the other hand, the WNT(dV/dR_{AZ}) is notably positive or increasing during restoration phases but shows no significant variation during deterioration phases before $\Delta_t = +2$ h (Figs. 12b,d, red curve).

These observations indicate that 1) while the radial structure evolves smoothly and in conjunction with intensity, as observed on case studies in section 4b, the WNT(Vmax$_{AZ}$) variable has a better potential to anticipate strong intensity changes, and 2) the eyewall descriptor of asymmetry evolution, WNT(dV/dR_{AZ}), is also sensitive to RI and restorations, even with a slightly larger anticipation, but shows no connection to RW and deterioration of intensity, possibly due to the more transient and random character of eyewall dynamics (Van Sang et al. 2008). Positive trends denote a process of axisymmetrization and merging of polarized asymmetric perturbation around vortex center, which is associated with the restoration and increase of the bulk vortex intensity. On the other hand, negative trends indicate the reinforcement of strong low wavenumber asymmetry within the vortex and the instability of the convective ring. While the maximum wind ring appears to be able to capture these prominent variations in the asymmetry and stability of the convective and vortical structure, the eye–eyewall radial gradient appears too transient in nature for such diagnoses.

The radial parameters moreover seem limited in terms of predictability as they only diagnose the bulk structure state of the vortex and thus can only help knowing its current intensity, stability, or intensification regime. On the other hand, WNT(Vmax$_{AZ}$) has the potential to be a good diagnosis of ongoing intensity modulations, and to infer the prediction of rapid intensifications and weakenings, or even of restoration and deterioration events throughout the life cycle. To further assess the predictability
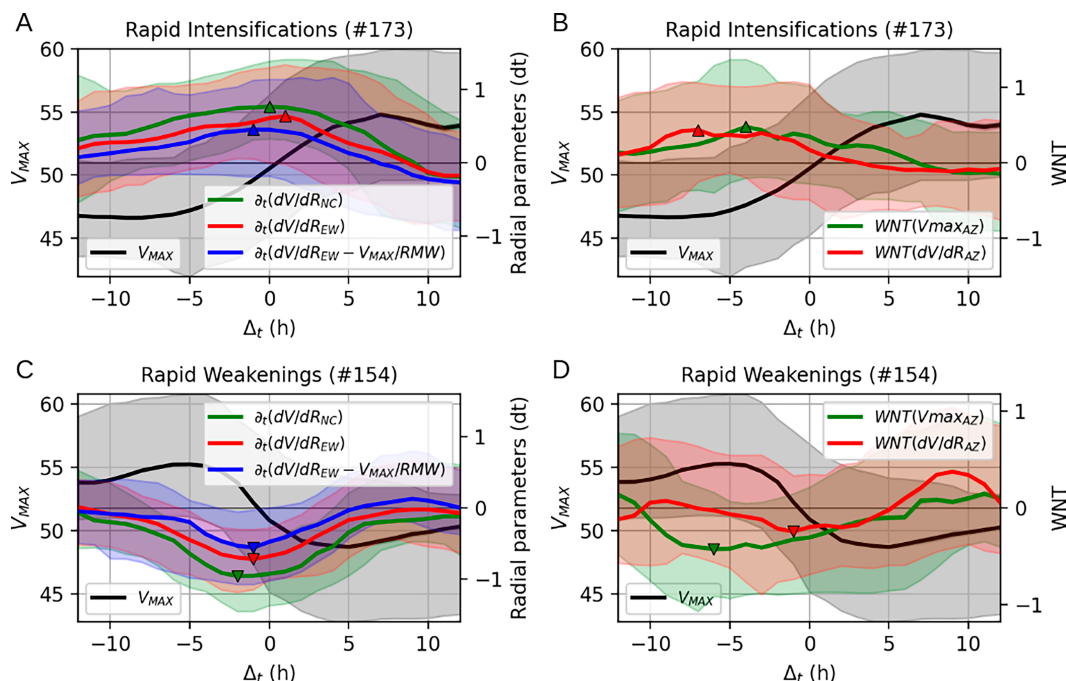
FIG. 11. Median composites of internal structure parameters over all events of (top) rapid intensification (RI) and (bottom) rapid weakening (RW), with the time lag around the event indicated on the x axis. RI phases are defined as time steps where the time derivative of V_{MAX} smoothed with a 12-h cutoff period is above 15 m s^{-1} day^{-1}, and RW phases under -15 m s^{-1} day^{-1}. (left) Time derivatives of dV/dR_{NC} (green), dV/dR_{EW} (red), and $dV/dR_{\text{EW}} - V_{\text{MAX}}/\text{RMW}$ (blue) along with V_{MAX} (black). (right) Values of WNT(Vmax$_{\text{AZ}}$) (green) and WNT(dV/dR_{AZ}) (red). Solid curves show the mean and dotted curves show the lower and upper quartiles of each composite. Maxima (top) and minima (bottom) are denoted by triangle markers.

potential of these different variables, we assess in the next section the contribution of these variables in the classification of positive and negative intensification rates.

d. Prediction score improvement including internal structure evolution

The machine learning classification method described in section 2f was applied to model outputs in order to complement the characterization of interactions between internal structure and intensity variations, taking into account nonlinear interactions and a larger amount of variables altogether. The classification method was designed to dissociate intensifying and weakening TCs, with target groups defined as intensification rates above 5 m s^{-1} day^{-1} and under -5 m s^{-1} day^{-1}. The classifications are performed using subgroups of 4 variables taken among instantaneous mean vortex parameters (i.e., latitude, maximum wind, RMW, and eyewall radial gradient), time-dependent structural parameters (i.e., time derivatives of mean radial gradients, explained variance by WN groups, or spectral low-to-high WNT for the two azimuthal signals), and a random control variable.

The sensitivity to the time scale used to define intensification is assessed by performing the classification over intensification rates computed on time series smoothed with filters at 12, 24, and 48 h. Results are summarized in Fig. 13, showing the five best prediction scores compared to a control combination of instantaneous

variables (i.e., V_{MAX} + RMW + latitude + random, first score on the left). Combinations including time derivative of the radial and azimuthal structural parameters significantly improve the score compared to the control combination by at least 11% for all intensification smoothings. Slightly higher scores and improvements (up to 13%) are achieved when considering a much smoother intensification rate.

To evaluate the parameters contributing the most to the classification, the number of occurrences of each variable among the 10 best combinations is counted (Fig. 14). The absolute latitude and time derivative of dV/dR_{NC} appear in all the 10 best combinations, and for all smoothing periods, meaning these two variables are the best contributors to the classification. This, not surprisingly, indicates the predominance of synoptic and vortex-scale dynamics as drivers of intensification phases. Latitude is a good descriptor of the TC's life cycle at the first order: intensification usually occurs at low latitudes while weakening goes with the higher atmospheric shear and colder sea surface temperature present at higher latitudes at the end of the TC life cycle. The near-core gradient was also expected as a good descriptor as it was spotted as highly correlated to the intensity in section 4b.

The following most contributing parameter is WNT(Vmax$_{\text{AZ}}$) (present in 6 of the 10 best combinations). This supports the above results showing a good correlation of cumulative WNT(Vmax$_{\text{AZ}}$) and intensity, and composites of intensification
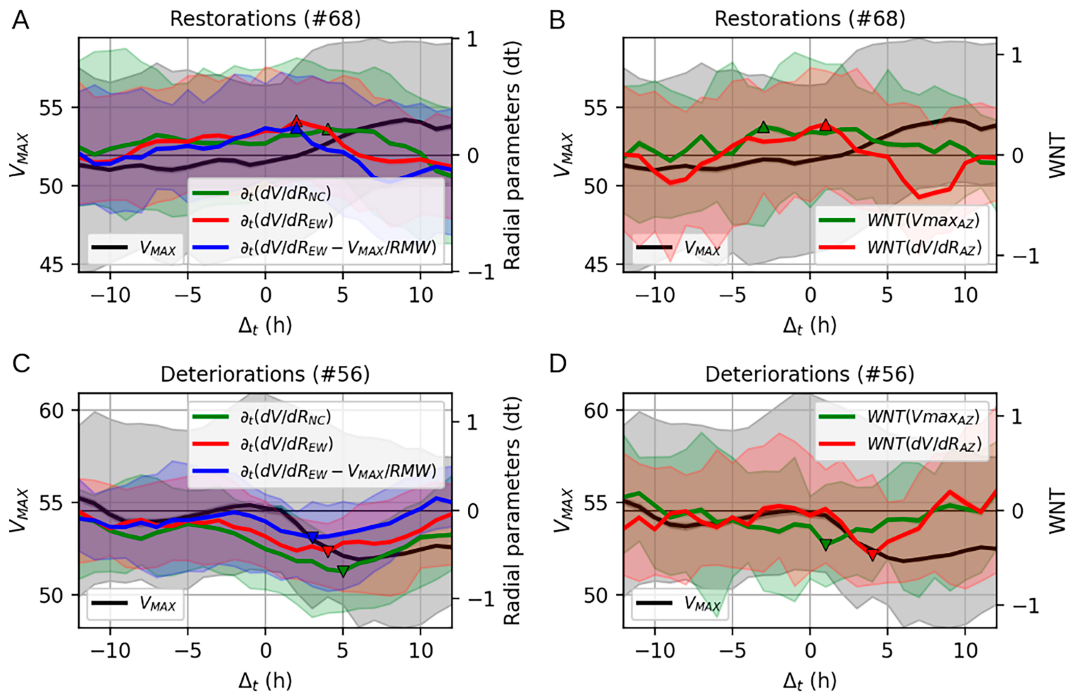
FIG. 12. As in Fig. 11, but for events of fast restoration and fast deterioration. Restoration events are defined as simulations time steps where the smoothed V_{MAX} time series (12-h cutoff period) is at a local maximum of its second derivative (i.e., local maximum of intensity acceleration) and followed by a phase of positive intensification rate. Deterioration events are defined conversely at local minima of V_{MAX} second derivative followed by a negative intensification rate.

phases. Its role as a predominant predictor thus indicates that the classifier is sensitive to the azimuthal variability and balance in WN distribution within the ring of maximum winds. For a smoothing of 48 h in intensification, this predictor is less present (only 3 occurrences over the 10 best combinations) highlighting, here again, that variations in the wind field asymmetry and

spectral distribution are more connected to short-scale intensity variations than to the overall TC life cycle scale.

The lower contributions of V_{MAX} and RMW and of other internal structure variables (i.e., eyewall radial wind gradient, instantaneous radial gradients, WNT(Vmax$_{AZ}$) and WNs 6–180 explained variances) show that the information contained
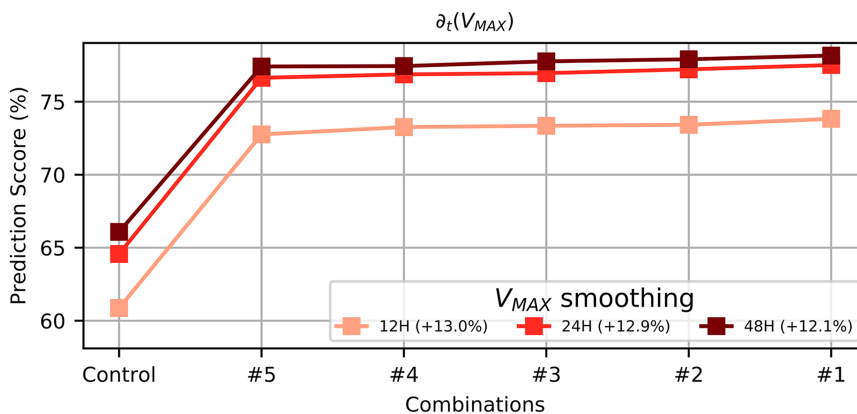

FIG. 13. Prediction scores for the classification of positive and negative $\partial_t(V_{\mathrm{MAX}})$ (i.e., intensifications and weakenings, respectively) for the control combination V_{MAX} + RMW + latitude + random (on the left) and for the 5 best scores obtained by integrating internal structure time-derivative predictors. The different curves denote the values obtained for intensifications/weakenings computed with different smoothing applied to the V_{MAX} signal (cutoff period between 12 and 48 h). The relative difference between the control and the best combination scores is written in the legend.
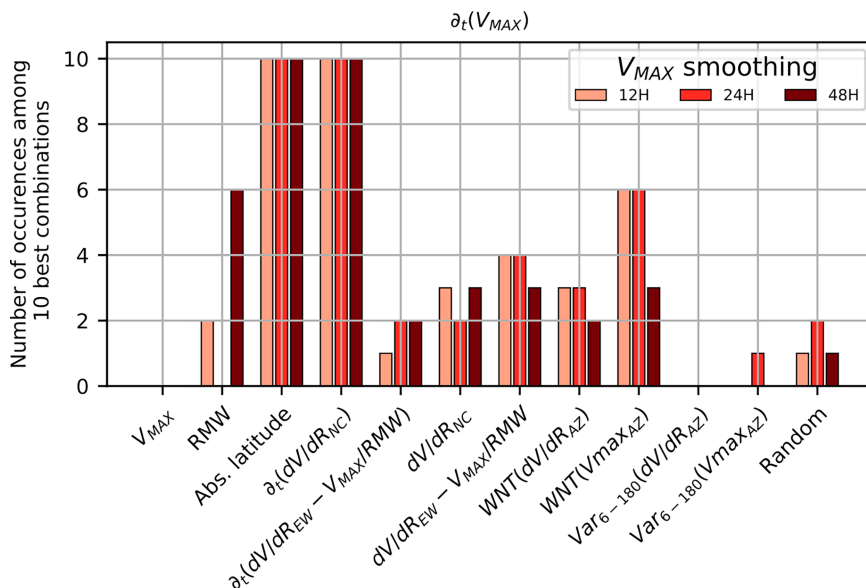
$$\partial_t(V_{MAX})$$

FIG. 14. Bar plot showing the number of occurrences (y axis) of each variable (x axis) among the 10 best combinations retrieved from the classification of positive/negative $\partial_t(V_{\mathrm{MAX}})$, for different values of smoothing (same color code as Fig. 13).

5. Summary and discussion

In this study, seven major TC cases (reaching at least category 4 during their life cycle) are simulated with the WRF Model at 1-km resolution thanks to a grid-nesting strategy using vortex-following moving nests. These simulations are designed to statistically evaluate the evolution of the TC surface wind field structure in relation with intensity variations. This work follows on a recent study by Vinour et al. (2021) showing that inner-core fine-scale asymmetry and radial profile diagnostics retrieved from SAR imagery have the potential to improve the statistical predictability of TC intensification rates compared to synoptic/mean vortex parameters only. Here we evaluate the added value of having the temporal evolution of the wind field structure, and particularly its fine scales, to further analyze the connections between vortex internal changes, and TC intensity modulation.

The TC surface wind field is thus described in this study with 3 kinds of parameters: the mean-vortex parameters (V_{MAX}, RMW, latitude), the mean wind-profile parameters (eyewall and near-core radial gradients), and the azimuthal asymmetry parameters (azimuthal wavenumber decomposition of eyewall wind gradient, and maximum wind ring intensity). The time evolution of these parameters is assessed through their time derivative or in the case of azimuthal asymmetry through a variable named wavenumber trend (WNT), which characterizes the concurrent and opposite evolution of

the variance explained by low and high WNs (respectively associated to vortex and local scale). Such parameters were designed to allow their diagnosis from SAR surface wind fields, and are shown to be good proxies of processes of axisymmetrization and vortex response to perturbations, such as internal mixing, merging, and organization of local potential vorticity inside the parent vortex which were depicted as the main drivers of TC dynamics in recent theoretical advances (Montgomery and Kallenbach 1997; Montgomery et al. 2006; Montgomery and Smith 2017; Smith et al. 2021).

The simulations fairly represent the average TC contraction with intensity, with a noted underestimation of the eyewall and near-core gradients, and an overestimation of the RMW for the strongest winds (category 4 and above). The azimuthal asymmetry of the eyewall gradient and the maximum wind ring are also realistically modeled, with only a slight shift toward a lower maximum wind variability than observed with SAR. The model limitations in featuring high values of maximum wind and radial gradients, small RMWs, and high asymmetry in the maximum wind contour may be attributable to the effective resolution of simulations (which is approximately 7 km, which is coarser than the 3-km resolution of SAR), to the model numerics, or to the model parameterizations. Several studies have shown that a small difference in spatial resolution can cause large discrepancies in the simulated maximum intensity and the featuring of small-scale variability (Fierro et al. 2009; Gentry and Lackmann 2010; Gopalakrishnan et al. 2011). Guimond et al. (2016b) and Hasan et al. (2022) also spotted a too strong numerical dissipation associated with the implicit scheme and notably the low-order spatial discretization of the pressure gradient, which significantly impacts the TC intensification. Intensity and intensification are also strongly sensitive to the microphysics, surface, and boundary

in these signals is less statistically useful for the diagnosis of intensity variations or redundant with other variables (e.g., RMW may be redundant with latitude as the TC size evolve with latitude).

layer parameterizations (Li and Pu 2008; Nolan et al. 2009a,b). Besides these limitations for highest winds, the model simulations are shown to realistically represent the TC's internal structure, its variability in time and space, as well as its intensity variations.

A comparison of the time spectra of extracted signals shows that the radial eyewall and near-core surface wind gradients evolve on a time scale similar to intensity, while azimuthal parameters, and especially the evolution in wind variance explained by local or vortex scales, are closer to the time scale of intensity variations. This suggests a separation between radial and azimuthal descriptors: while radial gradients tend to describe the state of the vortex, roughly following its maximum intensity, the azimuthal variability of the inner core has a larger connection with short-scale intensity changes, and is associated more to intensity modulations than to its magnitude.

The radial profile is observed to sharpen/contract when intensity increases and/or restores, while increased variance at small scale and concurrent decreased vortex-scale variance in the maximum wind ring are observed to precede phases of rapid intensification and restoration, and opposite behaviors are observed during rapid weakenings and deterioration of intensification.

This is consistent with previous studies associating, on one hand, the eyewall and maximum wind area distortions with barotropic instabilities and vorticity mixing disrupting the convection (Schubert et al. 1999; Kossin and Schubert 2001) and, on the other hand, restoration of intensity with symmetrization and homogenization of the vortex through vorticity merging and internal wave propagation (Montgomery and Kallenbach 1997; Montgomery et al. 2006). As described by the rotating-convection paradigm (Montgomery et al. 2006), energy transfers between local asymmetric scale and vortex symmetric scale are tightly related to the intensification and restoration of TC intensity. Although this paradigm was initially developed to describe the intensification of the vortex from a preexisting disturbance, i.e., the first stages of TC intensification, it is also applicable to mature intensity variations (Smith et al. 2021) and linked to other energetic axisymmetrization processes such as VRWs. The WN trends studied in this work are not equivalent to a kinetic energy cascade: according to Guimond et al. (2016b), such budget would require considering the diffusion and pressure gradient force contributions, which cannot be estimated from the surface wind field alone (and could not be estimated from observations). However, the present results manage to relate explicitly the variations of intensity to concurrent evolution of the asymmetric structure between polarized/vortex-scale and widespread/local-scale regimes. Our results further highlight that a metric such as the concurrent and opposite trend between large- and small-scale variance in the maximum wind ring may be a good proxy to anticipate intensity changes from high-resolution wind observations, suggesting a strong potential for forecast.

Although the time lag can vary significantly between cases, the observations made on case studies were confirmed by a statistical composite study of all rapid intensifications and weakenings, and restoration and deterioration of intensification over all

simulations. The maximum wind ring spectrum wavenumber trends indeed appear, averaged over all simulations, as slightly anticipating restoration and deterioration events by approximately 5–6 h.

The specificity of the maximum wind ring asymmetry for the diagnosis of ongoing and upcoming intensity was finally further highlighted by a machine learning classification of intensity variations. Overall, including time derivative of the radial and azimuthal structural parameters significantly improve the classification score (by at least 11%, and thus reaching about 75%) compared to considering only vortex-averaged parameters. The main contributors to the dissociation of phases of positive and negative intensification rates were the absolute latitude, the time derivative of near-core wind speed radial gradient, and the wavenumber trends of the maximum wind contour.

In contrast, the amplitude and asymmetry of the radial gradient between the eye and eyewall showed a slightly lower connection than expected with intensity changes (with intensification phases only). Indeed, a modification of the eye–eyewall surface wind profile can reveal a change of regime (Kossin and Eastin 2001) or, as described by Nguyen et al. (2011), a vacillation cycle of the eyewall, reflecting ongoing intensity changes. Yet, the classifier of intensification regimes clearly favored the near-core gradient rather than the eyewall gradient. This might indicate a mismatch between the studied time scales and variabilities: the mixing and vacillation cycles occur on typical time scales of 12 h in total, meaning the transition from one phase to another occurs within about 6 h, a time scale that is almost absent from intensity time series due to the applied 12-h cutoff period filter. This study was rather focused on persistent internal variations linked to marked intensity modulations (inferring the 12-h time-scale choice). It is most likely that a study of intensity variations at a finer time scale would help completing the causality chain between local short-scale perturbations of the wind field, eyewall convection, and vortex intensity modulations, although statistical consistency would be more difficult to obtain given the still limited number of samples and the large variability of the dataset.

Overall, this study strongly suggests that the diagnosis of several TC wind field parameters from available real-time observation sources could help improve intensity forecasts. In particular, the azimuthally averaged near-core radial wind gradient (between 1 and 3 times RMW) appears as a consistent proxy for TC intensity, and its sharpening/broadening is tightly connected to broad changes in TC intensity. This is an interesting perspective for operational forecast considering that this parameter can be easily measured from radiometers or scatterometers whereas accurate maximum wind speed estimates require a high resolution, as shown, for instance, by Combot et al. (2020) comparing radiometers to SAR estimates. The evolution of the maximum wind asymmetry distribution at vortex scale and local scale is noted as crucial. Although only partially describing the kinetic energy cascade going through the vortex, it is spotted as a consistent descriptor of ongoing and future intensity modulations, specifically rapid intensification and restoration events. As this variable is not measurable with precision from radiometers or scatterometers

due to their coarser resolution, this advocates for regular high-resolution observations of surface wind fields under TCs. A real-time operational measurement of azimuthal wavenumber trends in the maximum wind ring could certainly help bridging the gap encountered today in the meteorological forecast of TC intensity.

Data availability statement. The numerical simulations on which this paper is based are too large to be retained or publicly archived with available resources. All the information needed to replicate the simulations are provided in section 2; we used model version (V3.7.1). The model code is available at https://www.mmm.ucar.edu/models/wrf. Compilation script, initial and boundary condition files, and the detailed namelist settings can be provided by the corresponding author at Ifremer.

REFERENCES

Abarca, S. F., and K. L. Corbosiero, 2011: Secondary eyewall formation in WRF simulations of Hurricanes Rita and Katrina (2005). *Geophys. Res. Lett.*, **38**, L07802, https://doi.org/10.1029/2011GL047015.

——, and M. T. Montgomery, 2013: Essential dynamics of secondary eyewall formation. *J. Atmos. Sci.*, **70**, 3216–3230, https://doi.org/10.1175/JAS-D-12-0318.1.

Bhalachandran, S., Z. S. Haddad, S. M. Hristova-Veleva, and F. D. Marks Jr., 2019: The relative importance of factors influencing tropical cyclone rapid intensity changes. *Geophys. Res. Lett.*, **46**, 2282–2292, https://doi.org/10.1029/2018GL079997.

Braun, S. A., M. T. Montgomery, and Z. Pu, 2006: High-resolution simulation of Hurricane Bonnie (1998). Part I: The organization of eyewall vertical motion. *J. Atmos. Sci.*, **63**, 19–42, https://doi.org/10.1175/JAS3598.1.

Combot, C., A. Mouche, J. Knaff, Y. Zhao, Y. Zhao, L. Vinour, Y. Quilfen, and B. Chapron, 2020: Extensive high-resolution synthetic aperture radar (SAR) data analysis of tropical cyclones: Comparisons with SFMR flights and best track. *Mon. Wea. Rev.*, **148**, 4545–4563, https://doi.org/10.1175/MWR-D-20-0005.1.

Corbosiero, K. L., and J. Molinari, 2002: The effects of vertical wind shear on the distribution of convection in tropical cyclones. *Mon. Wea. Rev.*, **130**, 2110–2123, https://doi.org/10.1175/1520-0493(2002)130<2110:TEOVWS>2.0.CO;2.

——, ——, A. R. Aiyyer, and M. L. Black, 2006: The structure and evolution of Hurricane Elena (1985). Part II: Convective asymmetries and evidence for vortex Rossby waves. *Mon. Wea. Rev.*, **134**, 3073–3091, https://doi.org/10.1175/MWR3250.1.

DeMaria, M., C. R. Sampson, J. A. Knaff, and K. D. Musgrave, 2014: Is tropical cyclone intensity guidance improving? *Bull. Amer. Meteor. Soc.*, **95**, 387–398, https://doi.org/10.1175/BAMS-D-12-00240.1.

Elsberry, R. L., T. S. Fraim, and R. N. Trapnell Jr., 1976: A mixed layer model of the oceanic thermal response to hurricanes. *J.*

Geophys. Res., **81**, 1153–1162, https://doi.org/10.1029/JC081i006p01153.

——, T. D. B. Lambert, and M. A. Boothe, 2007: Accuracy of Atlantic and eastern North Pacific tropical cyclone intensity forecast guidance. *Wea. Forecasting*, **22**, 747–762, https://doi.org/10.1175/WAF1015.1.

Emanuel, K., and F. Zhang, 2016: On the predictability and error sources of tropical cyclone intensity forecasts. *J. Atmos. Sci.*, **73**, 3739–3747, https://doi.org/10.1175/JAS-D-16-0100.1.

——, C. DesAutels, C. Holloway, and R. Korty, 2004: Environmental control of tropical cyclone intensity. *J. Atmos. Sci.*, **61**, 843–858, https://doi.org/10.1175/1520-0469(2004)061<0843:ECOTCI>2.0.CO;2.

Fierro, A. O., R. F. Rogers, F. D. Marks, and D. S. Nolan, 2009: The impact of horizontal grid spacing on the microphysical and kinematic structures of strong tropical cyclones simulated with the WRF-ARW model. *Mon. Wea. Rev.*, **137**, 3717–3743, https://doi.org/10.1175/2009MWR2946.1.

Foster, R. C., 2005: Why rolls are prevalent in the hurricane boundary layer. *J. Atmos. Sci.*, **62**, 2647–2661, https://doi.org/10.1175/JAS3475.1.

Frank, W. M., and E. A. Ritchie, 2001: Effects of vertical wind shear on the intensity and structure of numerically simulated hurricanes. *Mon. Wea. Rev.*, **129**, 2249–2269, https://doi.org/10.1175/1520-0493(2001)129<2249:EOVWSO>2.0.CO;2.

Gentry, M. S., and G. M. Lackmann, 2010: Sensitivity of simulated tropical cyclone structure and intensity to horizontal resolution. *Mon. Wea. Rev.*, **138**, 688–704, https://doi.org/10.1175/2009MWR2976.1.

Ginis, I., 2002: Tropical cyclone-ocean interactions. *Adv. Fluid Mech.*, **33**, 83–114.

Gopalakrishnan, S. G., F. Marks Jr., X. Zhang, J.-W. Bao, K.-S. Yeh, and R. Atlas, 2011: The experimental HWRF system: A study on the influence of horizontal resolution on the structure and intensity changes in tropical cyclones using an idealized framework. *Mon. Wea. Rev.*, **139**, 1762–1784, https://doi.org/10.1175/2010MWR3535.1.

Guimond, S. R., G. M. Heymsfield, P. D. Reasor, and A. C. Didlake Jr., 2016a: The rapid intensification of Hurricane Karl (2010): New remote sensing observations of convective bursts from the Global Hawk platform. *J. Atmos. Sci.*, **73**, 3617–3639, https://doi.org/10.1175/JAS-D-16-0026.1.

——, J. M. Reisner, S. Marras, and F. X. Giraldo, 2016b: The impacts of dry dynamic cores on asymmetric hurricane intensification. *J. Atmos. Sci.*, **73**, 4661–4684, https://doi.org/10.1175/JAS-D-16-0055.1.

——, J. A. Zhang, J. W. Sapp, and S. J. Frasier, 2018: Coherent turbulence in the boundary layer of Hurricane Rita (2005) during an eyewall replacement cycle. *J. Atmos. Sci.*, **75**, 3071–3093, https://doi.org/10.1175/JAS-D-17-0347.1.

——, P. D. Reasor, G. M. Heymsfield, and M. M. McLinden, 2020: The dynamics of vortex Rossby waves and secondary eyewall development in Hurricane Matthew (2016): New insights from radar measurements. *J. Atmos. Sci.*, **77**, 2349–2374, https://doi.org/10.1175/JAS-D-19-0284.1.

Guinn, T. A., and W. H. Schubert, 1993: Hurricane spiral bands. *J. Atmos. Sci.*, **50**, 3380–3403, https://doi.org/10.1175/1520-0469(1993)050<3380:HSB>2.0.CO;2.

Hasan, M. B., S. R. Guimond, M. L. Yu, S. Reddy, and F. X. Giraldo, 2022: The effects of numerical dissipation on hurricane rapid intensification with observational heating. *J. Adv. Model. Earth Syst.*, **14**, e2021MS002897, https://doi.org/10.1029/2021MS002897.

Hazelton, A. T., R. E. Hart, and R. F. Rogers, 2017: Analyzing simulated convective bursts in two Atlantic hurricanes. Part II: Intensity change due to bursts. *Mon. Wea. Rev.*, **145**, 3095–3117, https://doi.org/10.1175/MWR-D-16-0268.1.

Huang, L., X. Li, B. Liu, J. A. Zhang, D. Shen, Z. Zhang, and W. Yu, 2018: Tropical cyclone boundary layer rolls in synthetic aperture radar imagery. *J. Geophys. Res. Oceans*, **123**, 2981–2996, https://doi.org/10.1029/2018JC013755.

Judt, F., and S. S. Chen, 2015: A new aircraft hurricane wind climatology and applications in assessing the predictive skill of tropical cyclone intensity using high-resolution ensemble forecasts. *Geophys. Res. Lett.*, **42**, 6043–6050, https://doi.org/10.1002/2015GL064609.

——, and ——, 2016: Predictability and dynamics of tropical cyclone rapid intensification deduced from high-resolution stochastic ensembles. *Mon. Wea. Rev.*, **144**, 4395–4420, https://doi.org/10.1175/MWR-D-15-0413.1.

Kelley, O. A., and J. B. Halverson, 2011: How much tropical cyclone intensification can result from the energy released inside of a convective burst? *J. Geophys. Res.*, **116**, D20118, https://doi.org/10.1029/2011JD015954.

Kilroy, G., R. K. Smith, and M. T. Montgomery, 2016: Why do model tropical cyclones grow progressively in size and decay in intensity after reaching maturity? *J. Atmos. Sci.*, **73**, 487–503, https://doi.org/10.1175/JAS-D-15-0157.1.

Kimball, S. K., 2006: A modeling study of hurricane landfall in a dry environment. *Mon. Wea. Rev.*, **134**, 1901–1918, https://doi.org/10.1175/MWR3155.1.

Knapp, K. R., M. C. Kruk, D. H. Levinson, H. J. Diamond, and C. J. Neumann, 2010: The International Best Track Archive for Climate Stewardship (IBTrACS) unifying tropical cyclone data. *Bull. Amer. Meteor. Soc.*, **91**, 363–376, https://doi.org/10.1175/2009BAMS2755.1.

Kossin, J. P., and M. D. Eastin, 2001: Two distinct regimes in the kinematic and thermodynamic structure of the hurricane eye and eyewall. *J. Atmos. Sci.*, **58**, 1079–1090, https://doi.org/10.1175/1520-0469(2001)058<1079:TDRITK>2.0.CO;2.

——, and W. H. Schubert, 2001: Mesovortices, polygonal flow patterns, and rapid pressure falls in hurricane-like vortices. *J. Atmos. Sci.*, **58**, 2196–2209, https://doi.org/10.1175/1520-0469(2001)058<2196:MPFPAR>2.0.CO;2.

Kuo, H.-C., R. T. Williams, and J.-H. Chen, 1999: A possible mechanism for the eye rotation of Typhoon Herb. *J. Atmos. Sci.*, **56**, 1659–1673, https://doi.org/10.1175/1520-0469(1999)056<1659:APMFTE>2.0.CO;2.

——, L.-Y. Lin, C.-P. Chang, and R. T. Williams, 2004: The formation of concentric vorticity structures in typhoons. *J. Atmos. Sci.*, **61**, 2722–2734, https://doi.org/10.1175/JAS3286.1.

——, W. H. Schubert, C.-L. Tsai, and Y.-F. Kuo, 2008: Vortex interactions and barotropic aspects of concentric eyewall formation. *Mon. Wea. Rev.*, **136**, 5183–5198, https://doi.org/10.1175/2008MWR2378.1.

Lewis, B. M., and H. F. Hawkins, 1982: Polygonal eye walls and rainbands in hurricanes. *Bull. Amer. Meteor. Soc.*, **63**, 1294–1300, https://doi.org/10.1175/1520-0477(1982)063<1294:PEWARI>2.0.CO;2.

Li, Q., and Y. Wang, 2012: A comparison of inner and outer spiral rainbands in a numerically simulated tropical cyclone. *Mon. Wea. Rev.*, **140**, 2782–2805, https://doi.org/10.1175/MWR-D-11-00237.1.

Li, X., and Z. Pu, 2008: Sensitivity of numerical simulation of early rapid intensification of Hurricane Emily (2005) to cloud microphysical and planetary boundary layer parameterizations.

Mon. Wea. Rev., **136**, 4819–4838, https://doi.org/10.1175/2008MWR2366.1.

——, J. A. Zhang, X. Yang, W. G. Pichel, M. DeMaria, D. Long, and Z. Li, 2013: Tropical cyclone morphology from spaceborne synthetic aperture radar. *Bull. Amer. Meteor. Soc.*, **94**, 215–230, https://doi.org/10.1175/BAMS-D-11-00211.1.

Macdonald, N. J., 1968: The evidence for the existence of Rossby-like waves in the hurricane vortex. *Tellus*, **20A**, 138–150, https://doi.org/10.3402/tellusa.v20i1.9993.

Mallen, K. J., M. T. Montgomery, and B. Wang, 2005: Reexamining the near-core radial structure of the tropical cyclone primary circulation: Implications for vortex resiliency. *J. Atmos. Sci.*, **62**, 408–425, https://doi.org/10.1175/JAS-3377.1.

Menelaou, K., M. K. Yau, and Y. Martinez, 2013a: Impact of asymmetric dynamical processes on the structure and intensity change of two-dimensional hurricane-like annular vortices. *J. Atmos. Sci.*, **70**, 559–582, https://doi.org/10.1175/JAS-D-12-0192.1.

——, ——, and ——, 2013b: On the origin and impact of a polygonal eyewall in the rapid intensification of Hurricane Wilma (2005). *J. Atmos. Sci.*, **70**, 3839–3858, https://doi.org/10.1175/JAS-D-13-091.1.

Möller, J. D., and M. T. Montgomery, 1999: Vortex Rossby waves and hurricane intensification in a barotropic model. *J. Atmos. Sci.*, **56**, 1674–1687, https://doi.org/10.1175/1520-0469(1999)056<1674:VRWAHI>2.0.CO;2.

Montgomery, M. T., and R. J. Kallenbach, 1997: A theory for vortex Rossby-waves and its application to spiral bands and intensity changes in hurricanes. *Quart. J. Roy. Meteor. Soc.*, **123**, 435–465, https://doi.org/10.1002/qj.49712353810.

——, and R. K. Smith, 2014: Paradigms for tropical cyclone intensification. Naval Postgraduate School Dept. of Meteorology Tech. Rep., 33 pp.

——, and ——, 2017: Recent developments in the fluid dynamics of tropical cyclones. *Annu. Rev. Fluid Mech.*, **49**, 541–574, https://doi.org/10.1146/annurev-fluid-010816-060022.

——, M. E. Nicholls, T. A. Cram, and A. B. Saunders, 2006: A vortical hot tower route to tropical cyclogenesis. *J. Atmos. Sci.*, **63**, 355–386, https://doi.org/10.1175/JAS3604.1.

Morrison, I., S. Businger, F. Marks, P. Dodge, and J. A. Businger, 2005: An observational case for the prevalence of roll vortices in the hurricane boundary layer. *J. Atmos. Sci.*, **62**, 2662–2673, https://doi.org/10.1175/JAS3508.1.

Mouche, A. A., B. Chapron, B. Zhang, and R. Husson, 2017: Combined co- and cross-polarized SAR measurements under extreme wind conditions. *IEEE Trans. Geosci. Remote Sens.*, **55**, 6746–6755, https://doi.org/10.1109/TGRS.2017.2732508.

——, ——, J. Knaff, Y. Zhao, B. Zhang, and C. Combot, 2019: Copolarized and cross-polarized SAR measurements for high-resolution description of major hurricane wind structures: Application to Irma category 5 hurricane. *J. Geophys. Res. Oceans*, **124**, 3905–3922, https://doi.org/10.1029/2019JC015056.

Muramatsu, T., 1986: The structure of polygonal eye of a typhoon. *J. Meteor. Soc. Japan*, **64**, 913–921, https://doi.org/10.2151/jmsj1965.64.6_913.

Nguyen, M. C., M. J. Reeder, N. E. Davidson, R. K. Smith, and M. T. Montgomery, 2011: Inner-core vacillation cycles during the intensification of Hurricane Katrina. *Quart. J. Roy. Meteor. Soc.*, **137**, 829–844, https://doi.org/10.1002/qj.823.

Nolan, D. S., J. A. Zhang, and D. P. Stern, 2009a: Evaluation of planetary boundary layer parameterizations in tropical cyclones by comparison of in situ observations and high-resolution simulations of Hurricane Isabel (2003). Part I: Initialization,

maximum winds, and the outer-core boundary layer. *Mon. Wea. Rev.*, **137**, 3651–3674, https://doi.org/10.1175/2009MWR 2785.1.

——, D. P. Stern, and J. A. Zhang, 2009b: Evaluation of planetary boundary layer parameterizations in tropical cyclones by comparison of in situ observations and high-resolution simulations of Hurricane Isabel (2003). Part II: Inner core boundary layer and eyewall structure. *Mon. Wea. Rev.*, **137**, 3675–3698, https://doi.org/10.1175/2009MWR2786.1.

Price, J. F., 1981: Upper ocean response to a hurricane. *J. Phys. Oceanogr.*, **11**, 153–175, https://doi.org/10.1175/1520-0485 (1981)011<0153:UORTAH>2.0.CO;2.

Reasor, P. D., M. T. Montgomery, and L. D. Grasso, 2004: A new look at the problem of tropical cyclones in vertical shear flow: Vortex resiliency. *J. Atmos. Sci.*, **61**, 3–22, https://doi. org/10.1175/1520-0469(2004)061<0003:ANLATP>2.0.CO;2.

——, M. D. Eastin, and J. F. Gamache, 2009: Rapidly intensifying Hurricane Guillermo (1997). Part I: Low-wavenumber structure and evolution. *Mon. Wea. Rev.*, **137**, 603–631, https://doi.org/10.1175/2008MWR2487.1.

Rogers, R., 2010: Convective-scale structure and evolution during a high-resolution simulation of tropical cyclone rapid intensification. *J. Atmos. Sci.*, **67**, 44–70, https://doi.org/10.1175/ 2009JAS3122.1.

——, P. Reasor, and S. Lorsolo, 2013: Airborne Doppler observations of the inner-core structural differences between intensifying and steady-state tropical cyclones. *Mon. Wea. Rev.*, **141**, 2970–2991, https://doi.org/10.1175/MWR-D-12-00357.1.

——, ——, and J. A. Zhang, 2015: Multiscale structure and evolution of Hurricane Earl (2010) during rapid intensification. *Mon. Wea. Rev.*, **143**, 536–562, https://doi.org/10.1175/MWR-D-14-00175.1.

Rotunno, R., Y. Chen, W. Wang, C. Davis, J. Dudhia, and G. J. Holland, 2009: Large-eddy simulation of an idealized tropical cyclone. *Bull. Amer. Meteor. Soc.*, **90**, 1783–1788, https://doi. org/10.1175/2009BAMS2884.1.

Rozoff, C. M., and J. P. Kossin, 2011: New probabilistic forecast models for the prediction of tropical cyclone rapid intensification. *Wea. Forecasting*, **26**, 677–689, https://doi.org/10.1175/ WAF-D-10-05059.1.

——, W. H. Schubert, B. D. McNoldy, and J. P. Kossin, 2006: Rapid filamentation zones in intense tropical cyclones. *J. Atmos. Sci.*, **63**, 325–340, https://doi.org/10.1175/JAS3595.1.

Schecter, D. A., M. T. Montgomery, and P. D. Reasor, 2002: A theory for the vertical alignment of a quasigeostrophic vortex. *J. Atmos. Sci.*, **59**, 150–168, https://doi.org/10.1175/1520-0469(2002)059<0150:ATFTVA>2.0.CO;2.

Schubert, W. H., M. T. Montgomery, R. K. Taft, T. A. Guinn, S. R. Fulton, J. P. Kossin, and J. P. Edwards, 1999: Polygonal eyewalls, asymmetric eye contraction, and potential vorticity mixing in hurricanes. *J. Atmos. Sci.*, **56**, 1197–1223, https:// doi.org/10.1175/1520-0469(1999)056<1197:PEAECA>2.0. CO;2.

Shapiro, L. J., and H. E. Willoughby, 1982: The response of balanced hurricanes to local sources of heat and momentum. *J. Atmos. Sci.*, **39**, 378–394, https://doi.org/10.1175/1520-0469(1982) 039<0378:TROBHT>2.0.CO;2.

Skamarock, W. C., and J. B. Klemp, 2008: A time-split nonhydrostatic atmospheric model for weather research and forecasting applications. *J. Comput. Phys.*, **227**, 3465–3485, https://doi. org/10.1016/j.jcp.2007.01.037.

Smith, R. K., W. Ulrich, and G. Sneddon, 2000: On the dynamics of hurricane-like vortices in vertical-shear flows. *Quart. J.*

Roy. Meteor. Soc., **126**, 2653–2670, https://doi.org/10.1002/qj. 49712656903.

——, M. T. Montgomery, and N. Van Sang, 2009: Tropical cyclone spin-up revisited. *Quart. J. Roy. Meteor. Soc.*, **135**, 1321–1335, https://doi.org/10.1002/qj.428.

——, G. Kilroy, and M. T. Montgomery, 2021: Tropical cyclone life cycle in a three-dimensional numerical simulation. *Quart. J. Roy. Meteor. Soc.*, **147**, 3373–3393, https://doi.org/10.1002/qj. 4133.

Steranka, J., E. B. Rodgers, and R. C. Gentry, 1986: The relationship between satellite measured convective bursts and tropical cyclone intensification. *Mon. Wea. Rev.*, **114**, 1539–1546, https://doi.org/10.1175/1520-0493(1986)114<1539:TRBSMC> 2.0.CO;2.

Stern, D. P., J. L. Vigh, D. S. Nolan, and F. Zhang, 2015: Revisiting the relationship between eyewall contraction and intensification. *J. Atmos. Sci.*, **72**, 1283–1306, https://doi.org/10.1175/ JAS-D-14-0261.1.

Van Sang, N., R. K. Smith, and M. T. Montgomery, 2008: Tropical-cyclone intensification and predictability in three dimensions. *Quart. J. Roy. Meteor. Soc.*, **134**, 563–582, https://doi. org/10.1002/qj.235.

Velden, C. S., C. Rozoff, A. Wimmers, M. Sitkowski, M. E. Kieper, J. Kossin, J. Hawkins, and J. Knaff, 2010: An objective method to predict near real time rapid intensification of tropical cyclones using satellite passive microwave observations. *29th Conf. on Hurricanes and Tropical Meteorology*, Tucson, AZ, Amer. Meteor. Soc., P1.53, https://ams.confex. com/ams/29Hurricanes/techprogram/paper_167742.htm.

Vinour, L., S. Jullien, A. Mouche, C. Combot, and M. Mangeas, 2021: Observations of tropical cyclone inner-core fine-scale structure, and its link to intensity variations. *J. Atmos. Sci.*, **78**, 3651–3671, https://doi.org/10.1175/JAS-D-20-0245.1.

Vukicevic, T., E. Uhlhorn, P. Reasor, and B. Klotz, 2014: A novel multiscale intensity metric for evaluation of tropical cyclone intensity forecasts. *J. Atmos. Sci.*, **71**, 1292–1304, https://doi. org/10.1175/JAS-D-13-0153.1.

Wang, H., Y. Wang, and H. Xu, 2013: Improving simulation of a tropical cyclone using dynamical initialization and large-scale spectral nudging: A case study of Typhoon Megi (2010). *Acta Meteor. Sin.*, **27**, 455–475, https://doi.org/10.1007/s13351-013-0418-y.

Wang, Y., 2002a: Vortex Rossby waves in a numerically simulated tropical cyclone. Part I: Overall structure, potential vorticity, and kinetic energy budgets. *J. Atmos. Sci.*, **59**, 1213–1238, https://doi.org/10.1175/1520-0469(2002)059<1213:VRWIAN> 2.0.CO;2.

——, 2002b: Vortex Rossby waves in a numerically simulated tropical cyclone. Part II: The role in tropical cyclone structure and intensity changes. *J. Atmos. Sci.*, **59**, 1239–1262, https:// doi.org/10.1175/1520-0469(2002)059<1239:VRWIAN>2.0. CO;2.

——, 2008: Rapid filamentation zone in a numerically simulated tropical cyclone. *J. Atmos. Sci.*, **65**, 1158–1181, https://doi.org/ 10.1175/2007JAS2426.1.

——, 2009: How do outer spiral rainbands affect tropical cyclone structure and intensity? *J. Atmos. Sci.*, **66**, 1250–1273, https:// doi.org/10.1175/2008JAS2737.1.

Wu, L., H. Su, R. G. Fovell, T. J. Dunkerton, Z. Wang, and B. H. Kahn, 2015: Impact of environmental moisture on tropical cyclone intensification. *Atmos. Chem. Phys.*, **15**, 14041–14053, https://doi.org/10.5194/acp-15-14041-2015.